DEPARTMENT OF DEFENSE
UNITED STATES OF AMERICA

3 Aug 2002

DEPARTMENT OF THE AIR FORCE
EUROPEAN OFFICE OF AEROSPACE RESEARCH AND DEVELOPMENT (EOARD)

AMORPHOUS SILICON PHOTONIC MICROCAVITIES

EOARD Special Contract SPC 01-4062
Contract Order Number F61775-01-WE062

Final Report

DISTRIBUTION STATEMENT A
Approved for Public Release
Distribution Unlimited

Dr. Ali Serpengüzel, Principal Investigator
Koc University, Microphotonics Research Laboratory
Department of Physics, Rumeli Feneri Yolu
Science Building, Sariyer 34450 Istanbul - Turkey

Voice: +90 (212) 338-1312
Facsimile: +90 (212) 338-1547
E-mail: aserpenguzel@ku.edu.tr
URL: http://microphotonics.ku.edu.tr

AQ F03-05-1020

REPORT DOCUMENTATION PAGE	Form Approved OMB No. 0704-0188

maintaining the data needed, and completing and reviewing the collection of information. Send comments regarding this burden estimate or any other aspect of this collection of information, including suggestions for reducing the burden, to Department of Defense, Washington Headquarters Services, Directorate for Information Operations and Reports (0704-0188), 1215 Jefferson Davis Highway, Suite 1204, Arlington, VA 22202-4302. Respondents should be aware that notwithstanding any other provision of law, no person shall be subject to any penalty for failing to comply with a collection of information if it does not display a currently valid OMB control number.
PLEASE DO NOT RETURN YOUR FORM TO THE ABOVE ADDRESS.

1. REPORT DATE ***(DD-MM-YYYY)***	**2. REPORT TYPE** Final Report	**3. DATES COVERED** *(From – To)* 3 August 2001 - 03-Aug-02

4. TITLE AND SUBTITLE Amorphous Silicon Photonic Microcavities	**5a. CONTRACT NUMBER** F61775-01-WE062
	5b. GRANT NUMBER
	5c. PROGRAM ELEMENT NUMBER
6. AUTHOR(S) Dr. Ali Serpenguzel	**5d. PROJECT NUMBER**
	5d. TASK NUMBER
	5e. WORK UNIT NUMBER

7. PERFORMING ORGANIZATION NAME(S) AND ADDRESS(ES) Koc University Rumeli Feneri Yolu, Science Building, Room 161 Sariyer 80910 Turkey	**8. PERFORMING ORGANIZATION REPORT NUMBER** N/A
9. SPONSORING/MONITORING AGENCY NAME(S) AND ADDRESS(ES) EOARD PSC 802 BOX 14 FPO 09499-0014	**10. SPONSOR/MONITOR'S ACRONYM(S)**
	11. SPONSOR/MONITOR'S REPORT NUMBER(S) SPC 01-4062

12. DISTRIBUTION/AVAILABILITY STATEMENT

Approved for public release; distribution is unlimited.

13. SUPPLEMENTARY NOTES

14. ABSTRACT

This report results from a contract tasking Koc University as follows: The contractor will investigate the use of microcavities to control photoluminescence in amorphous silicon. This can lead to significant improvements in luminescent displays, optical sensors, and optoelectronic devices. Amorphous siliconis of special interest since the material is abundant and inexpensive.

15. SUBJECT TERMS

EOARD, optics, Photonics, Laser physics

16. SECURITY CLASSIFICATION OF:			**17. LIMITATION OF ABSTRACT**	**18, NUMBER OF PAGES**	**19a. NAME OF RESPONSIBLE PERSON**
a. REPORT UNCLAS	**b. ABSTRACT** UNCLAS	**c. THIS PAGE** UNCLAS	UL	65	Alexander J. Glass, Ph. D.
					19b. TELEPHONE NUMBER *(Include area code)* +44 (0)20 7514 4953

Standard Form 298 (Rev. 8/98)
Prescribed by ANSI Std. Z39-18

Physics & Astronomy Classification Scheme (PACS)* codes:

(71.23.Cq) Amorphous semiconductors, metallic glasses, glasses;
(73.61.Jc) Amorphous semiconductors; glasses;
(78.66.Jg) Amorphous semiconductors; glasses; nanocrystalline materials;
(78.55.-m) Photoluminescence.

*http://www.aip.org

Optics Classification & Indexing Scheme (OCIS) codes:**

(050.2230) Fabry-Perot;
(230.0250) Optoelectronics;
(230.1480) Bragg reflector;
(230.5750) Resonators;
(250.5230) Photoluminescence;
(300.2530) Laser induced fluorescence,
(310.0310) Thin films;
(310.2790) Guided waves.

**http://www.osa.org

Keywords:

Amorphous silicon,
Distributed Bragg reflector,
Guided waves,
Fabry-Perot,
Microcavity,
Optoelectronics,
Photoluminescence,
Resonators,
Spontaneous emission,
Thin films.

Preface

The report comprises the results obtained from the 'Amorphous Silicon Photonic Microcavities' EOARD Special Contract SPC 01-4062, Contract Order Number F61775-01-WE062. The purpose of this project is to investigate the use of photonic microcavities to control the photoluminescence in amorphous silicon. This can lead to significant improvements in luminescent displays, optical sensors, and optoelectronic devices.

In this research, properties of bulk and microcavity hydrogenated amorphous silicon nitride are studied. Microcavities were realized by embedding the active hydrogenated amorphous silicon layer between two metallic or dielectric mirrors. The dielectric mirrors were realized with two distributed Bragg reflectors (DBR's). The DBR's are one dimensional photonic bandgap (PBG) materials, i.e., photonic crystals, composed of alternating layers of silicon oxide and silicon nitride. All of the layers are grown by plasma enhanced chemical vapor deposition (PECVD) on silicon substrates. The temperature dependence of the amorphous silicon photoluminescence is performed to fully characterize and optimize the material in the pursuit of obtaining novel photonic microdevices. Photonics device characterization was done by means of atomic force microscopy (AFM), scanning electron microscopy (SEM), photoluminescence, and reflectance measurements. The reflectance spectra calculations were performed using the transfer matrix method (TMM).

Properties of amorphous silicon, photonic microcavities, and PBG materials are introduced in Chapter 1. Amorphous silicon is studied in detail in Chapter 2. A general theoretical background of the photonic microcavities and the definitions of the fundamental microcavity parameters are given in Chapter 3. Chapter 4 includes the considerations taken into account, while designing the microcavity structures and the fabrication process. In Chapter 5, the techniques used for characterizing the structures, as well as the results of the measurements, and calculations are presented. Finally, Chapter 6 concludes the work.

As the principal investigator of this project, I would like to acknowledge the support of our Laboratory engineer, Adnan Kurt, and my graduate students Temel Bilici, Senol Isci, Ibrahim Inanç, and Selim Tanriseven.

Istanbul, November, 2002 *Ali Serpengüzel*

Contents

List of Figures

List of Tables

1. Introduction

1.1. Amorphous silicon

In the optoelectronics and microelectronics industry silicon is the most widely used semiconductor, not only in its crystalline, but also in its amorphous form. Being a direct band-gap material, [1] unlike crystalline silicon, [2] amorphous silicon is unmatched as a photoreceptor for laser printing, for switching elements in large area liquid crystal displays, for large photovoltaic panels, and any other application that calls for a high quality semiconductor that can be processed on large areas or on curved or flexible substrates. It is generally agreed that the terms amorphous solid, non-crystalline solid, disordered solid, glass, or liquid have no precise structural meaning beyond the description that, the structure is not crystalline on any significant scale. The principal structural order present is imposed by the approximately constant separation of nearest-neighbor atoms or molecules.

Until the early 1970's, amorphous silicon prepared by evaporation or sputtering was not considered as one of the valuable semiconductor materials, because of high density of electronic states in the band gap related to a large density of structural defects. [3] The discovery of an amorphous silicon material prepared by the glow discharge deposition of silane, which can be doped and whose conductivity can be changed by ten orders of magnitude marked a turning point and opened a new research area.

Most interest focused on hydrogenated amorphous silicon and its alloys, since hydrogen by removing dangling bonds eliminates non-radiative recombination centers, that are responsible for reduced luminescence efficiency (and reduced photovoltaic efficiency) and allows doping. [4] Another advantage of the hydrogenated amorphous silicon is that, it can be deposited by plasma enhanced chemical vapor deposition (PECVD) onto almost any substrate at temperatures below 500 K, which makes it compatible with the microelectronic technology.

1.2. Photonic microcavities

Photonic microcavities are currently experiencing a boom. Together with the complimentary microstructures of photonic bandgap (PBG) materials, these microresonators attract the attention of the scientists and engineers in the field of optics and photonics. As we enter the information age, the photonic microcavities is the building block of the communication revolution. There are basically two major communities, who are interested in these optical microcavities. The atomic physics and condensed matter physics communities approach these optical microstructures with the scientific and basic research interest. For the physicists, the main interest in these optical microstructures is for their ability to sustain high optical fields, and therefore strongly interact with the material with which the optical microresonator is constructed from. The optoelectronics community however has a purely technological interest and approaches these optical resonators with an applied research interest. The optical communication engineers would like to manufacture high efficiency light sources such as lasers and light emitting diodes, and photodetectors for dense wavelength division multiplexing applications for optical fiber communication.

From an historical perspective, we can label the birth of the first optical resonator with the invention of the first optical interference spectroscope by Charles Fabry and Alfred Perot in 1899. Another major breakthrough happened in 1946 when E. M. Purcell proposed the use of electromagnetic resonators for the manipulation of the density of states of the electromagnetic field modes.

Optical resonators with dimension of the order of an optical wavelength can now be fabricated in a variety of solid state systems including semiconductors, organic materials, and glasses. [5] Ideally, one can isolate a single optical mode of the optical field in a cube a half-wavelength on a side with perfectly reflecting walls. Liquid droplets, polymer spheres, and semiconductor microcavities with dielectric mirrors are examples of microcavities with which, one can approach this ideal limit, and nearly isolate a few modes of the electromagnetic spectrum from the continuum of the surrounding freespace modes.

The simplest approach to fabricate an optical microcavity is to shrink the spacing between the mirrors of a Fabry-Perot resonator to a half wavelength. This structure provides a single dominant longitudinal mode, that radiates into a narrow range of angles around the cavity axis. The interaction of optically active material with isolated modes in the cavity offers interesting physical systems for basic studies and a rich variety of possible applications. Interactions between atoms and low-loss optical and microwave cavities have led to the demonstrations of cavity quantum electrodynamics effects, (QED) including coupled atom-cavity modes, quantum revivals, single-atom masers, and enhanced or inhibited spontaneous emission (SE).

Microcavity resonators have the potential to provide low-cost, efficient, and high-density optoelectronic light sources over a broad range of the spectrum, from the near-infrared to well into the visible. They can be used as very efficient light emitting diodes and low threshold microlasers. [6] In any macroscopic laser, SE is a major source of energy loss, speed limitation and noise. The fraction of the SE that is coupled into a single lasing mode can be increased by the enhancement and of SE by the microcavity. The efficiency emission rates, and photon statistics of light emitting diodes can all be controlled by forming microcavity resonators with sufficiently high quality factors. Control of these properties will be welcome in a number of optoelectronic applications including flat panel electroluminescent displays and optical interconnects.

1.3. Photonic bandgap materials

The concept of Bragg reflection was recognized by the 1915 Nobel Prize awarded jointly to W. Henry Bragg and his son W. Lawrence Bragg 'for their services in the analysis of crystal structure by means of X-rays.' The optical application of Bragg Scattering was analyzed for the first time by P. Rouard in 1937 using multiple transparent optical layers. However, these one dimensional distributed Bragg reflectors (DBR's) were used only as band reject optical filters and their potential has not been fully realized, until Eli Yablonovitch and Sajev John independently proposed in 1987 the concept of three dimensional photonic crystals or Photonic bandgap (PBG's) materials.

The PBG idea is borrowed from solid state physics, where electronic bandgaps exist for an electronic crystal structure, and prevent the existence of electronic levels at certain energies. Currently, this microscopic branch of photonics and optoelectronics is experiencing a rapid and exciting development and growth. PBG materials are constructed by spatially patterning the dielectric function of a medium in a periodic way. A medium engineered in such a way exhibits photonic stop bands, i.e., PBG's, for a certain range of frequencies of the electromagnetic spectrum. A PBG structure can also be treated as a photonic crystal constructed from "photonic atoms", i.e., dielectric "photonic resonators", which possess electromagnetic resonances at discrete frequencies. Photonic atoms are the electromagnetic analogue of the real "electronic" atoms, which possess electronic resonances at discrete frequencies. The distributed Bragg reflectors used in the amorphous silicon microcavities are examples of one-dimensional PBG's.

1.4. References

[1] J.D. Joannopoulos and G. Lucovsky, "The physics of hydrogenated amorphous silicon," (Springer Verlag, Berlin, 1984).

[2] S. Perkowitz, "Optical Characterization of Semiconductors," (Academic Press, London, 1993), p.27.

[3] P. Shaoqi and D. Xiaoning, "Properties of Sputtered Amorphous Silicon without Hydrogen", in "*Proceedings of the International Workshop on Amorphous Semiconductors,*" H. Fritzsche, D. Han, C. C. Tsai, Eds. (World Scientific, Singapore, 1987).

[4] J. I. Panvoke, "Luminescence in Hydrogenated Amorphous Silicon", in "*Proceedings of the International Workshop on Amorphous Semiconductors,*" H. Fritzsche, D. Han, C. C. Tsai, Eds., (World Scientific, Singapore, 1987).

[5] Y. Yamamoto and R. E. Slusher, "Optical Processes in Microcavities," Phys. Today, **46**, 66 (1993).

[6] R. E. Slusher and C. Weisbuch, "Optical Microcavities in Condensed Matter Systems," Solid State. Commun., **92**, 149 (1994).

2. Amorphous Silicon

Interest in silicon (Si) as a material for optoelectronics has increased recently. With modern process techniques, it will be possible to integrate lasers, photodetectors, and waveguides into optoelectronic silicon motherboards to route and modulate optical signals within such silicon motherboards. Integrated silicon optoelectronics is a rapidly developing field [7]. Discrete and integrated devices such as photodetectors, modulators, light emitters, resonant cavity enhanced (RCE) photodetectors, waveguides, photonic bandgap filters, optical amplifiers, optical interconnects, and optoelectronic integrated circuits are already being realized. However, most of these devices, with the exception of light emitters, are fabricated using crystalline silicon. Light emission requires the use of amorphous silicon, since crystalline silicon can not emit light due to its indirect bandgap.

Hydrogenated amorphous silicon (a-Si:H) is already an established material in semiconductor technology [8]. The major application of a-Si:H is photovoltaics, color detectors, and active matrix displays. The primary attribute of the technology is its large area capability, which is unavailable with other technologies. Another advantage of a-Si:H is that, it can be deposited by plasma enhanced chemical vapor deposition (PECVD) on almost any substrate at temperatures below 500 K, which makes it compatible with the microelectronic technology. This property justifies the interest in a-Si:H as a potential optoelectronic material. Planar waveguides are already being realized from a-Si:H [9]. With modern process techniques, it will be possible to integrate lasers, photodetectors, and waveguides into Si motherboards [10,11] for wavelength division multiplexing (WDM) applications [12].

2.1. Luminescence of amorphous silicon

The advantage of a-Si:H, as well as porous silicon (π-Si), is that, they attract interest as a potential optical gain medium, because of their room temperature visible electroluminescence (EL) and photoluminescence (PL). Planar microcavity effects on the PL of π-Si [13] as well as Si/SiO$_x$ superlattices [14] have already been reported. Recently, we have observed visible PL from a-Si:H, as well as its oxides (a-SiO$_x$:H) and nitrides (a-SiN$_x$:H) grown by low temperature PECVD. [15] While the exact mechanism of the occurrence of the PL in bulk a-SiN$_x$:H is still under discussion, the quantum confinement model is a widely accepted. [16] In the quantum confinement model the material consist of small a-Si clusters in a matrix of a-SiN$_x$:H. The regions with Si-H and Si-N, having larger energy gaps due to strong Si-H and Si-N bonds, isolate these a-Si clusters, and form barrier regions around them. The PL originates from the a-Si clusters.

A-SiN$_x$:H can be grown both with and without ammonia (NH_3). The samples grown without NH_3 are referred to as the Si rich samples. The luminescence of these samples is in the red-near-infrared part of the optical spectrum. The samples grown with NH_3 and annealed at 800° C are referred to as the nitrogen rich samples. The luminescence of these samples is in the blue-green part of the optical spectrum [17]. The following figure shows the room temperature PL of silicon rich a-SiN_x:H grown without NH_3. The PL spectrum has a linewidth of 250 nm and the peak of the PL is at 710 nm.

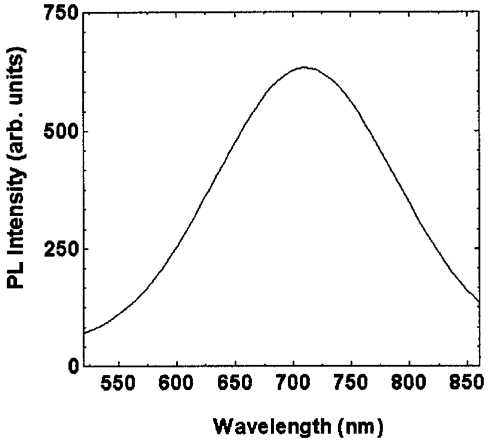

Figure 2.1. Room temperature photoluminescence of silicon rich a-SiN_x:H.

2.2. Surface morphology of the amorphous silicon

Atomic force microscopy (AFM) has been performed the on the a-SiN_x:H samples to characterize the morphology of the surface and to analyze origin of the luminescence. The surface of the a-SiN_x:H is optically flat and thus amenable for the growth of multiple layers. This is necessary condition for the realization of the one-dimensional PBG microcavity. The following figure shows a low resolution AFM of the a-SiNx:H surface.

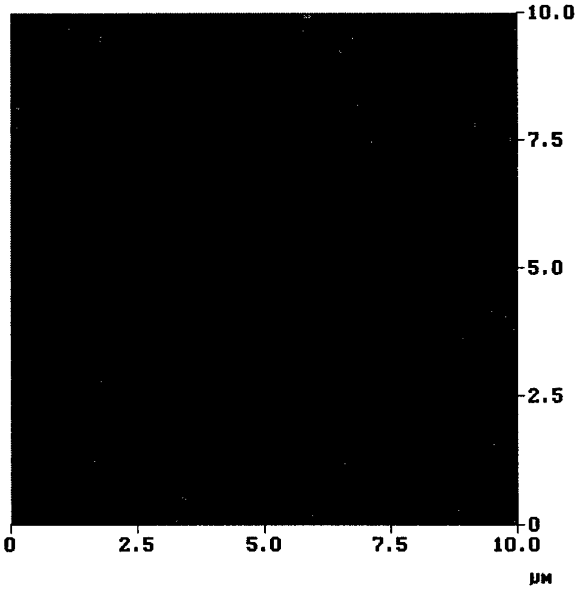

Figure 2.2. Low resolution AFM of the silicon rich a-SiNx:H surface.

The surface morphology of the a-SiNx:H is quite uniform. The bulk of the material is composed of globules of a-SiNx:H and is similar to π-Si, which has similar luminescence properties. The following figures show the medium and high resolution AFM pictures of the silicon rich a-SiNx:H surface. The similarity to π-Si can be observed better in these figures. Additionally, although the surface is flat optically, it is quite rough in the 100 nm range, which corresponds to the average globule size.

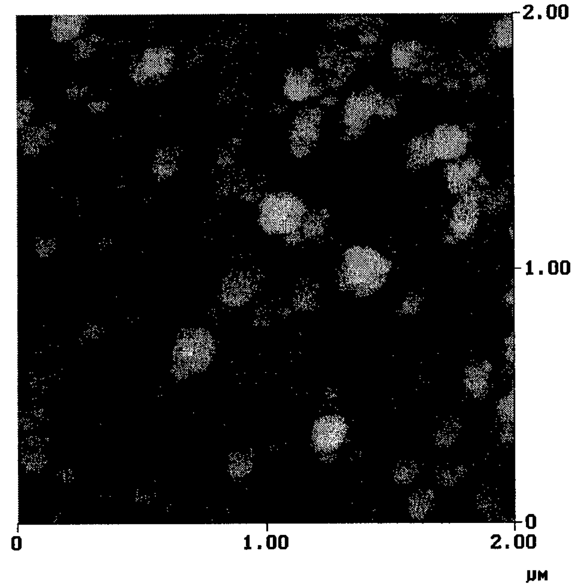

Figure 2.3. Medium resolution AFM of the silicon rich a-SiNx:H surface.

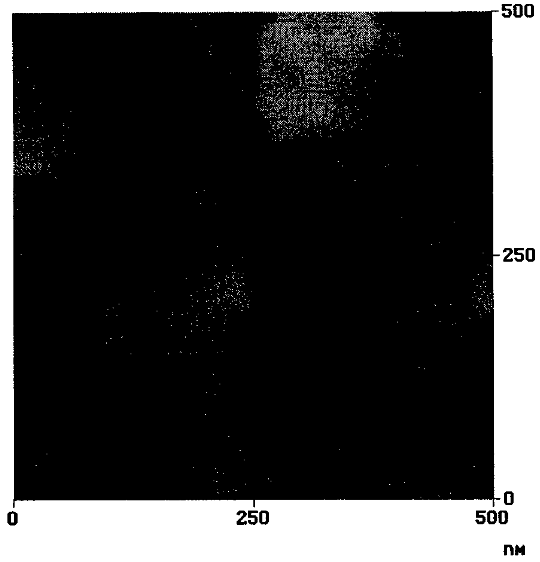

Figure 2.4.High resolution AFM of the silicon rich a-SiN_x:H surface.

2.3. Porous silicon

Similar to hydrogenated amorphous silicon (a-Si:H), porous silicon also exhibits room temperature visible PL [18]. Semiconductor microcavity effects have been applied to π-Si, after the observation of room temperature visible PL [19] made π-Si a potential optical gain medium [20]. Steady state [21, 22, 23] and temporally resolved, [24] single and multiple[25] microcavity controlled PL in π-Si has been observed experimentally [26, 27, 28] and calculated theoretically [29]. The possibility of using π-Si microcavities as chemical sensors has been investigated [30]. In addition, microcavity controlled PL has been observed in π-Si inorganic-organic structures [31], as well as Si/SiO_x superlattices [32, 33, 34]. SiO_2/TiO_2 microcavities [35], SiO_x/WO_y, and SiO_x/MO_y multilayers [36] have been fabricated. Microcavity controlled electroluminescence (EL) of π-Si has been reported [37, 38]. Interference filters [39] and optical waveguides [40] have also formed from π-Si. Two-dimensional (2-D) photonic crystals have been fabricated in π-Si [41] and silicon nitride (Si_3N_4) [42] waveguides.

2.4. References

[7] H. Zimmermann, “Integrated Silicon Optoelectronics,” (Springer Verlag, Berlin, 2000) pp. 1-352.

[8] R. A. Street, Ed., “Technology and Applications of Amorphous Silicon,” (Springer Verlag, Berlin, 2000), pp. 1-403.

[9] A. M. Agarwal, L. Liao, J. S. Foresi, M. R. Black, X. Duan, and L.C. Kimerling, "Low-loss Polycrystalline Silicon Waveguides for Silicon Photonics," J. Appl. Phys. **80**, 6120 (1996).

[10] B. Jalali, S. Yegnanarayanan, T. Yoon, T. Yoshimoto, I. Rendina, and F. Coppinger, "Advances in Silicon on insulator Optoelectronics," IEEE J. Select. Topics in Quantum Electron. **4**, 938 (1998).

[11] A. Kaneko, T. Goh, H. Yamada, T. Tanaka, and I. Ogawa “Design and applications of silica-based planar lightwave circuits,” IEEE J. Select. Topics in Quantum Electron. **5**, 1227 (1999).

[12] B. J. Offrein, R. Germann, F. Horst, H.W.M. Salemink, R. Beyerl, and G. L. Bona, “Resonant coupler-based tunable add-after-drop filter in silicon–oxynitride technology for WDM networks,” IEEE J. Select. Topics in Quantum Electron. **5**, 1400 (1999).

[13] L. Pavesi, R. Guardini, and C. Mazolleni, "Porous Silicon Resonant Cavity Light Emitting Diodes," Solid State Commun. **97**, 1051 (1996).

[14] B. T. Sullivan, D. J. Lockwood, H. J. Labbe, and Z.-H. Lu, "Photoluminescence in Amorphous Si/SiOx Superlattices Fabricated by Magnetron Sputtering," Appl. Phys. Lett. **69**, 3149 (1996).

[15] A. Serpengüzel, A. Aydinli, and A. Bek, "Enhancement and inhibition of photoluminescence in hydrogenated amorphous silicon nitride microcavities, " Optics Express **1**, 108 (1997).

[16] M. H. Brodsky, "Quantum Well Model of the Hydrogenated Amorphous Silicon," Solid State Commun. **36**, 55 - 59 (1980).

[17] A. Serpengüzel, A. Aydinli, A. Bek, and M. Güre, "Visible photoluminescence from planar amorphous silicon nitride microcavities, " J. Opt. Soc. Am. B. **15**, 2706 (1998).

[18] D. J. Wolford, B. A. Scoot, J. A. Reimer and J. A. Bradley, "Efficient visible luminescence from hydrogenated amorphous silicon," Physica **B 117**, 920 (1983).

[19] T. Canham, "Silicon Quantum Wire Array Fabrication by Electrochemical and Chemical Dissolution of Wafers," Appl. Phys. Lett. **57**, 1046 (1990).

[20] D. J. Lockwood, "Optical Properties of Porous Silicon," Solid State Commun. **92**, 101 (1994).

[21] L. Pavesi, C. Mazolleni, A. Tredicucci, and V. Pellegrini, "Controlled photon emission in porous silicon microcavities," Appl. Phys. Lett. **67**, 3280 (1995).

[22] L. Pavesi and V. Mulloni, “All porous silicon microcavities: growth and physics,” J. Lumin. **80**, 43 (1999).

[23] M. Araki, H. Koyama, and N. Koshida, "Precisely tuned emission from porous silicon vertical optical cavity in the visible region," J. Appl. Phys. **80**, 4841 (1996).

[24] M. Cazzanelli and L. Pavesi, "Time-resolved photoluminescence of all porous silicon microcavities," Phys. Rev. B **56**, 15264 (1997).

[25] E. K. Squire, P. A. Snow, P. St. J. Russell, L. T. Canham, A. J. Simmons, and C. L. Reeves, “Light emission from porous silicon single and multiple cavities,” J. Lumin. **80**, 125 (1999).

[26] M. Takahashi, Y. Toriumi, T. Matsumoto, Y. Masumoto, N. Koshida, “Significant photorefractive index change observed in porous silicon Fabry-Perot resonators,” Appl. Phys. Lett. **76**, 1990 (2000).

[27] S. Setzu, S. Letant, P. Solsona, R. Romestain, and J. C. Vial, “ Improvement of luminescence in p-type as-prepared or dye impregnated porous silicon microcavities,” J. Lumin. **80**, 129 (1999).

[28] Z. H. Xiong, S. Yuan, Z. M. Jiang, J. Qin, C. W. Pei L. S. Liao, X. M. Ding, X. Y. Hou, and X. Wang, "Photoluminescence studies of porous silicon microcavities," J. Lumin. **80**, 137 (1999).

[29] E. K. Squire, P. St. J. Russell, and P. A. Snow, "Optimized light emission from layered porous silicon structures," Appl. Opt. **37**, 7107 (1998).

[30] V. Mulloni and L. Pavesi, "Porous silicon microcavities as optical chemical sensors," Appl. Phys. Lett. **76**, 2523 (1999).

[31] A. Arena, S. Patane, G. Saitta, S. Savasta, R. Girlanda, and R. Rinaldi, "Silicon based organic-inorganic microcavity and its dispersion curve from angle resolved photoluminescence," Appl. Phys. Lett. **72**, 2571 (1998).

[32] B. T. Sullivan, D. J. Lockwood, H. J. Labbe, and Z.-H. Lu, "Photoluminescence in Amorphous Si/SiOx Superlattices Fabricated by Magnetron Sputtering," Appl. Phys. Lett. **69**, 3149 (1996).

[33] D. J. Lockwood, J.M. Baribeau, and B. T. Sullivan, "Visible light from Si/SiOx superlattices in planar microcavities," J. Vac. Sci. Technol. B **16**, 1707 (1998).

[34] D. J. Lockwood, B. T. Sullivan, and H. J. Labbe, "Visible light emission from Si/SiOx superlattices in optical microcavities," J. Lumin **80**, 75 (1999).

[35] K. M. Cheng, A. W. Sparks, H.-C. Luan, D. R. Lim, K. Wada, and L. C. Kimerling, "SiO2/TiO2 omnidirectional reflector and resonator with sol-gel method," Appl. Phys. Lett. **75**, 3805 (1999).

[36] F. Hamelmann, G. Haindl, J. Schmalhorst, A. Aschentrup, E. Majkova, U. Kleineberg, U. Heinzmann, A. Klipp, P. Jutzi, A. Anopchenko, M. Jergel, and S. Luby, "Metal oxide / silicon oxide multilayer with smooth interfaces produced by in situ controlled plasma enhanced MOCVD," Thin Solid Films **358**, 90 (2000).

[37] L. Pavesi, R. Guardini, and C. Mazolleni, "Porous Silicon Resonant Cavity Light Emitting Diodes," Solid State Commun. **97**, 1051 (1996).

[38] M. Araki, H. Koyama, and N. Koshida, "Controlled electroluminescence spectra of porous silicon diodes with vertical optical cavity," Appl. Phys. Lett. **69**, 2956 (1996).

[39] D. Hunkel, R. Butz, R. Ares-Fisher, M. Marso, and H. Lüth, "Interference filters from porous silicon with laterally varying wavelength of reflection," J. Lumin. **80**, 133 (1999).

[40] H. F. Arrand, T. M. Benson, P. Sewell, and A. Loni, "Optical waveguides in porous silicon pre-patterned by localized nitrogen implantation," J. Lumin. **80**, 199 (1999).

[41] S. W. Leonard, H. M. van Driel, K. Busch, S. John, A. Birner, A.-P. Li, F. Müller, U Gösele, and V. Lehmann, "Attenuation of optical transmission within the band gap of thin two-dimensional macroporous silicon photonic crystals," Appl. Phys. Lett. **75**, 3063 (1999).

[42] M. C. Netti, M. D. B. Charlton, G. J. Parker, and J. J. Baumberg, "Visible photonic band gap engineering in silicon nitride waveguides," Appl. Phys. Lett. **76**, 991 (2000).

3. Photonic Microcavity

An optical resonator, the optical counterpart of an electronic resonant circuit, confines and stores light at certain resonance frequencies. These specific frequencies correspond to the optical modes of the microcavity. The microcavity may be viewed as an optical transmission system incorporating feedback. Light circulates or is repeatedly reflected within the system. Using the right geometry it is possible to make one-, two-, or three dimensional optical resonators. Planar and spherical mirror resonators, ring resonators, and optical fiber resonators are the most typical optical resonators.

The simplest optical resonator is the planar mirror resonator, often called the Fabry-Perot resonator, which comprises two parallel planar mirrors between which light is repeatedly reflected with little loss. It was introduced by A. Fabry and Ch. Perot in 1899. The initial optical resonator was fabricated using two partially coated mirrors. Later on dielectric and semiconductor materials were also used, since the Fresnel reflections at high refractive index step at the material-air interface produces natural mirrors.

3.1. The Fabry-Perot cavity

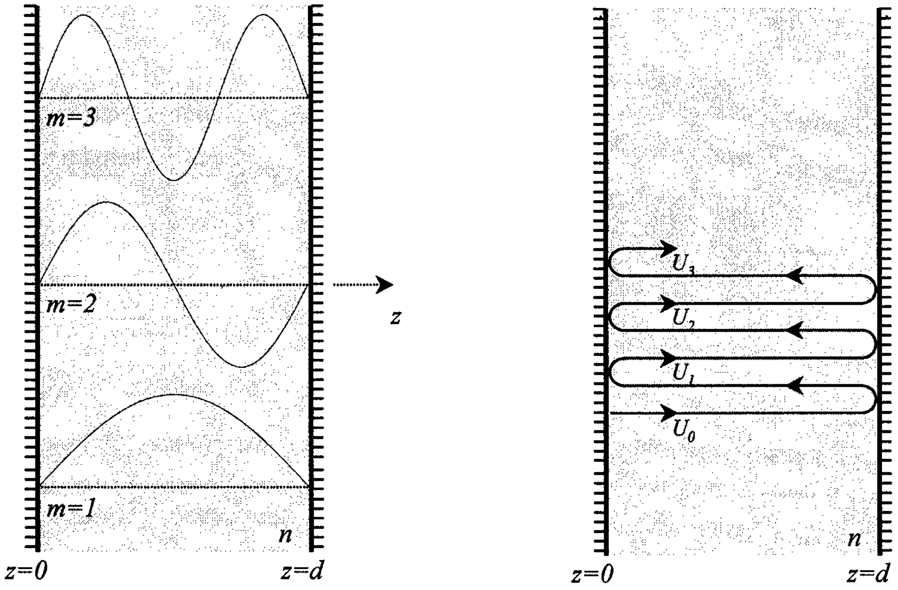

Figure 3.1.Schematic of a Fabry-Perot resonator with length d and refractive index n. The first three resonances are shown.

The first instrumental passive optical resonator was developed by Charles Fabry and Alfred Perot, and is now more than a century old. For an excellent review of the Fabry-Perot resonator the reader should consult the *Fabry-Perot Interferometer* by J. M. Vaughan [43]. The original paper on the *interference spectroscope* was published in the *Annales de Chimie et de Physique* in 1899 [44].

Additionally, a summary paper focusing on the spectroscopic and metrological applications was also published [45] together with an English translation [46]. The previous figure is a schematic description of the Fabry-Perot resonator, and the circulation of photons caused by the reflection from the mirrors forming the cavity.

3.2. Cavity Quantum Electrodynamics

In a microcavity, the photon density of states (DOS) are enhanced at the cavity resonances, when compared with the continuum of photon DOS of a bulk sample. The spontaneous emission (SE) cross-sections at the microcavity resonances are larger than the bulk SE cross-sections because of the enhanced photon DOS. Also, the luminescence cross-sections in between the microcavity resonances are smaller than the bulk SE cross-sections.

The cavity alteration of the SE was first proposed for radio waves. [47] The possibility to control the emission properties of materials with the use of optical microcavities [48,49] attracted the attention of the photonics community. [50,51] Afterwards, the microcavity alteration of the spontaneous emission was proposed [52] and observed in organic microcavities, [53] in the optical part of the electromagnetic spectrum. [54]

In addition, alteration of the SE in semiconductor microcavities was observed [55] and calculated. [56] In this weak coupling (of the photon and exciton modes) regime, the interaction (Rabi coupling) strength is smaller than the microcavity mode damping (linewidth) and the exciton mode damping (linewidth). The SE spectrum is altered due to a redistribution of the DOS by the presence of the microcavity. However, in the strong coupling (of the photon and exciton modes) regime, the interaction (Rabi coupling) strength is bigger than the microcavity mode damping (linewidth) and exciton mode damping (linewidth), and Rabi splitting of the microcavity and exciton modes occurs. [57] The proposition of strong coupling in optical microcavities, [58] was followed by its observation [59] and theory. [60]

If a cavity mode is probed out of the cavity, a resonant change of SE light intensity must be detected. This effect corresponding to a light intensity spatial redistribution is observed even in the absence of any sizeable resonant change of the average SE rate. [61] Since the lifetime changes are the most essential effect in the original concept of the modification of SE proposed by Purcell. [62] Much attention has been paid to the observation of the cavity induced changes of the SE decay rate. [63,64] However, the rate of change of SE lifetime in one dimensionally confined microcavity structures has been predicted theoretically to be relatively small. [65]

3.3. Optoelectronic Applications

Optical microcavities can now be realized in solid state systems such as organic materials [66] and semiconductors. [67] Semiconductor microcavities [68] are used in resonant cavity enhanced (RCE) optoelectronic devices, which are wavelength selective and ideal for wavelength division multiplexing (WDM) applications. [69] The simple planar Fabry-Perot resonator is the most widely used geometry in semiconductor microcavities.[70, 71] As they alter the optoelectronic properties of photonic gain media, semiconductor microcavities can be used in very low threshold lasers, and very efficient light emitting diodes (LED's). [72] Semiconductor microcavities have been used in the realization of the low threshold vertical cavity surface emitting lasers, [73, 74] external-cavity surface emitting lasers, [75] microdisk, [76] and microwire [77] lasers. Semiconductor microcavities have also been used in efficient RCE LED's. [78]

3.4. Resonator Modes

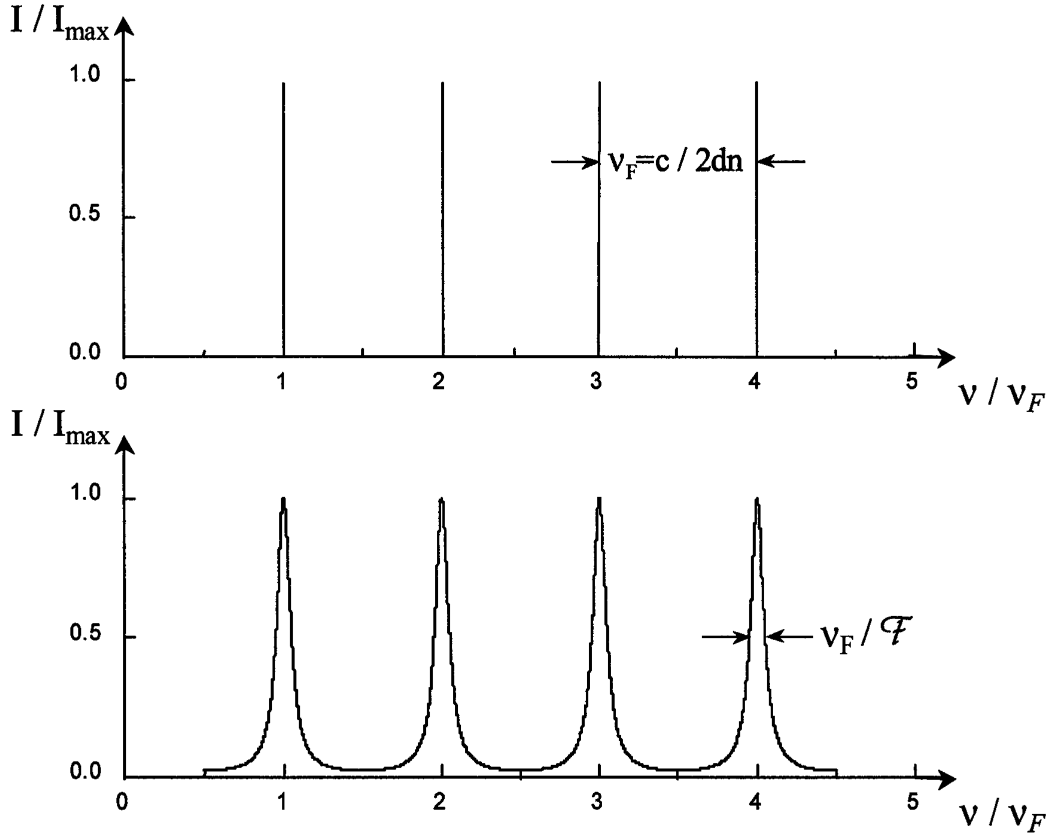

Figure 3.2.(a) A lossless resonator in the steady state can sustain light waves only at the precise resonance frequencies, (b) A lossy resonator sustains waves at all frequencies, but the attenuation resulting from the destructive interference increases at frequencies away from the resonances.

At resonance the length of the resonator is an integer number of half wavelengths. The resonator modes can alternatively be determined by following a wave as it travels back and forth between the two mirrors. A mode is a self reproducing wave, i.e., a wave that reproduces itself after a single roundtrip. The phase shift imparted by the two mirror reflections is 2π (π at each mirror). Only self-reproducing waves, or combinations of them, can exist within the resonator in the steady state. The strict condition on the frequencies of optical waves, that are permitted to exist inside a resonator, is relaxed when the resonator has losses.

The two principal source of loss in optical resonators are the absorption and scattering in the medium between the mirrors and the imperfect reflection at the mirrors. There are two underlying sources of reduced reflection; a partially transmitting mirror is often used in a resonator to permit the light to escape from it, and the finite size of the mirrors causes a fraction of the light to leak around the mirrors

In the previous figure (a) a lossless resonator in the steady state sustains light waves only at the precise resonance frequencies. A lossy resonator (b) sustains waves at all frequencies, however, the attenuation resulting from the destructive interference increases at frequencies away from the resonances.

The quality factor (*Q*) is often used to characterize electrical resonance circuits and resonators. Large *Q* factors are associated with low loss resonators. This parameter is defined as [79]:

$$Q = 2\pi \frac{(\text{stored energy})}{(\text{energy loss per cycle})}$$

3.5. Photonic Bandgap Materials

With the introduction of photonic bandgap (PBG) concept in 1987 independently by both Eli Yablonovitch [80] and Sajev John [81] suddenly other ways to fabricate microcavities appeared. PBG materials have indeed attracted much attention from the optics and optoelectronics community [82, 83, 84, 85]. PBG materials are constructed by spatially patterning the dielectric function of a medium in a periodic way. A medium engineered in such a way exhibits photonic stop bands, i.e., PBG's, for a certain range of frequencies of the electromagnetic spectrum. A PBG structure can also be treated as a photonic crystal constructed from "photonic atoms", i.e., dielectric "photonic resonators", which possess electromagnetic resonances at discrete frequencies. Photonic atoms are the electromagnetic analogue of the real "electronic" atoms, which possess electronic resonances at discrete frequencies. Historically, the PBG idea has been borrowed from solid state physics, where electronic bandgaps (EBG) exist for an electronic crystal structure, and prevent the existence of electronic levels at certain energies [86].

Alternatively, the PBG and the EBG can be categorized as the bandgaps associated with the electromagnetic field particle (photon) and the electromagnetic matter particle (electron). A one dimensional photonic atom is an optical cavity, where the electromagnetic waves are bounded in only one spatial dimension. After one round trip, the electromagnetic wave comes back to itself in phase. This is the most commonly used geometry in active optical devices such as lasers, and passive optical devices such as filters.

3.6. Distributed Bragg Reflector

The distributed Bragg reflector (DBR) is the simplest one-dimensional PBG. If electromagnetic radiation falls onto a structure consisting of thin films of several different materials, multiple reflections will take place within the structure. Exact analysis for the electromagnetic wave propagation in such structures can be done by the transfer matrix method (TMM). [87, 88, 89]

The simplest nontrivial periodic multilayer system to analyze is the one, whose period consists of two layers of differing refractive indices n_l, n_2 both having the same optical thickness. Such a system has a reflectance maximum at a wavelength, for which the optical thickness is a quarter wavelength and is called a simple quarter-wave stack or a distributed Bragg reflector (DBR).

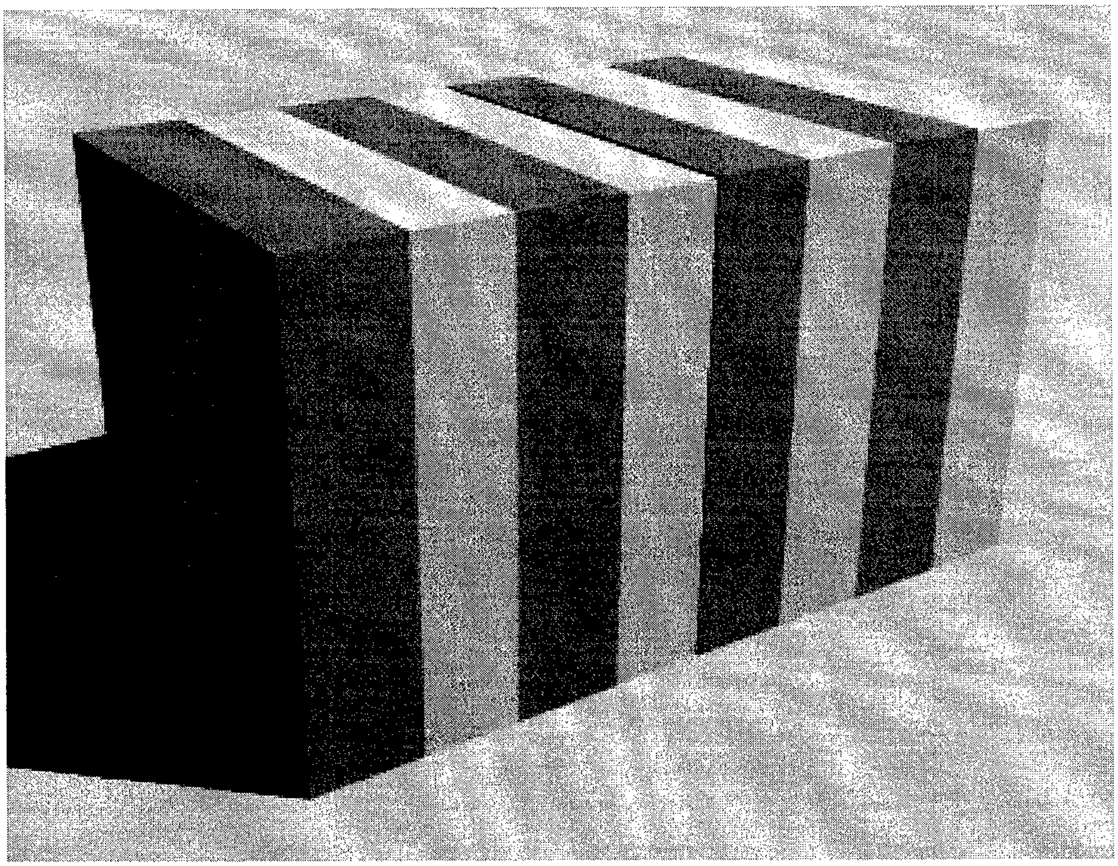

Figure 3.3. Schematic of an 8 layer distributed Bragg reflector (DBR)

The reflectance of a number of a-SiO$_x$:H and a-SiN$_x$:H quarter wave stacks, which are used as mirrors of the Fabry-Perot cavity, calculated by TMM is shown in the following figure as a function of the (normalized) reciprocal wavelength. This figure illustrates that, as the number (N) of periods in the stack increases, the reflectance at λ_o approaches unity. The transition from reflection to transmission becomes sharper, and the number of oscillations outside the rejection band increases. As N approaches infinity, the reflectance approaches unity over a band, i.e., the high reflectance zone [90]. For N = 7, N = 10 and N = 14, the reflectance maximum is 91, 97, and 99 %, respectively. The ratio n_L/n_H controls both the width and the height of the of the reflectance band.

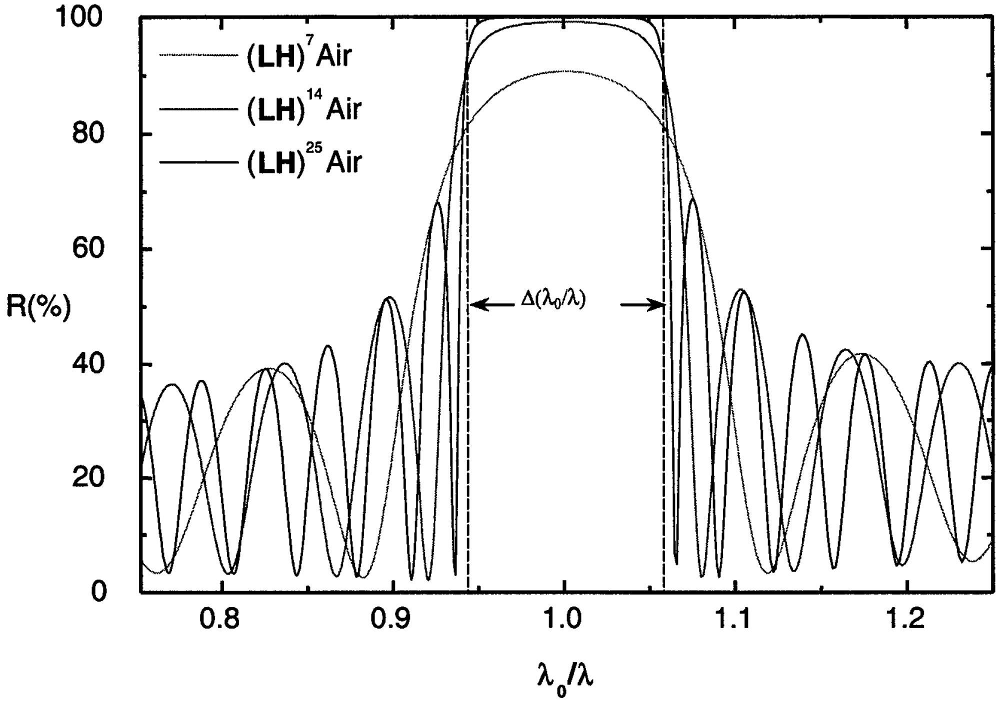

Figure 3.4. Calculated normalized reflectance spectra of 7, 14, 25 quarter-wave stack distributed Bragg reflectors (DBR's). L and H stand for low (a-SiO$_x$:H) and high (a-SiN$_x$:H) refractive index layers of quarter wave thickness at 710 nm.

3.7. The DBR Microcavity Analysis

A distributed Bragg reflector (DBR) microcavity is shown in the following figure. The DBR's are formed from alternating layers of low index ad high index passive optical material. The gain region is formed from a full wavelength thick active layer.

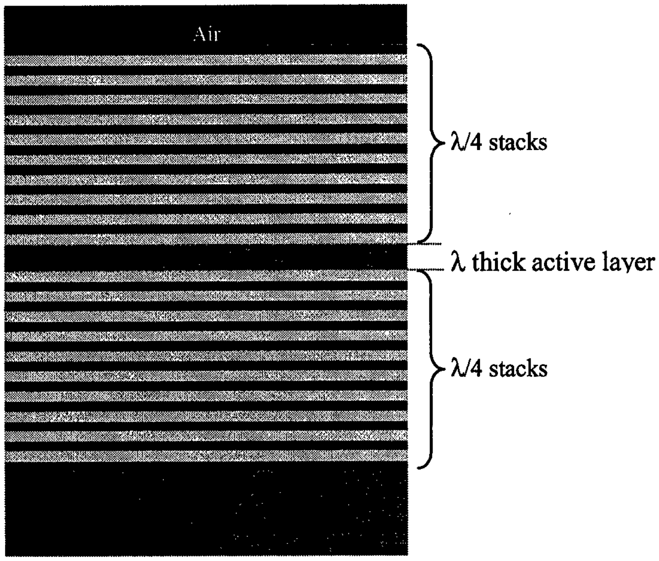

Figure 3.5. Schematic of an the amorphous silicon distributed Bragg reflector (DBR) photonic microcavity

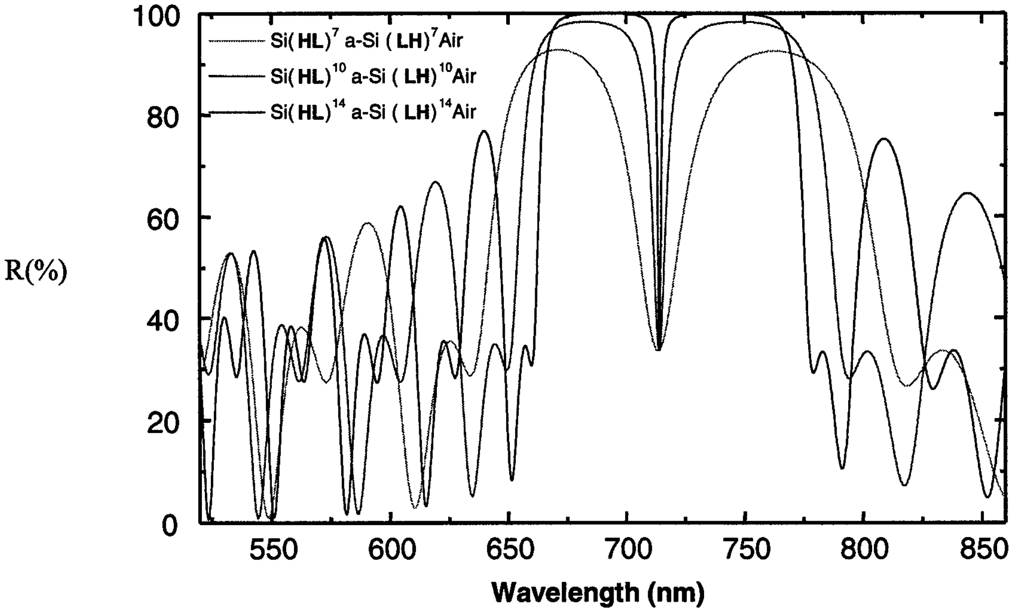

Figure 3.6. Calculated reflectance curves of microcavities with 7, 10, and 14 pairs of DBR layers on both sides L and H stand for low and high refractive index layers of quarter wave thickness at 710 nm.

The response of a number of microcavities with different number of periods in the quarter wave stack is shown in the previous figure. The calculations are performed by the transfer matrix method (TMM). This figure illustrates that, as the number of periods in the stack increases, the reflectance at λ_0 approaches unity. The transition from reflection to transmission becomes sharper, and the number of oscillations outside the rejection band increases. For N = 7, N = 10 and N = 14, the reflectance maximum is 91, 97, and 99 %, respectively. The ratio n_L/ n_H controls both the width and the height of the of the reflectance band. Additionally, as the reflectance of the mirrors increases, the resonant transmission bandwidth at the center design wavelenght of 710 nm decreases. The decrease of the resonant transmission bandwidth results in high quality factor resonances.

3.8. References

[43] J.M. Vaughan, "*The Fabry-Perot Interferometer: History, Theory, Practice, and Applications*," (Adam Hilger, Philadelphia, 1989) pp. 1-522.

[44] Ch. Fabry and A. Perot, "Theorie et applications d'une nouvelle methode de spectroscopie interferentielle," Ann. Chim. Phys. **16**, 115-144 (1899).

[45] A. Perot and Ch. Fabry, "Sur l'application de phenomenes d'interference a la solution de divers problemes de spectroscopie et de metrologie," Bulletin Astronomique **16**, 5-32 (1899).

[46] A. Perot and Ch. Fabry, "On the application of interference phenomena to the solutions of various problems of spectroscopy and metrology," Astrophysical Journal **9**, 87-115, (1899).

[47] E. M. Purcell, "Spontaneous Emission Probabilities at Radio Frequencies," Physical Review **69**, 681 (1946).

[48] K. H. Drexhage, "*Progress in Optics,*" Vol. 12, E. Wolf, Ed., (North-Holland, New York, 1974), p. 165.

[49] Y. Yamamoto, G. Bjork, H. Heitmann, and R. Horowicz, "Controlled Spontaneous Emission in Quantum Well Microcavities", in F. Henneberg, S.Schmitt-Rink, E. O. Gobel, Eds., "*Optics of Semiconductor Nanostructures,*" (Akademie Verlag, Berlin, 1993).

[50] J. Rarity and C. Weisbuch, Eds., "*Microcavities and Photonic Bandgaps: Physics and Applications*," (Kluver, Dordrecht, 1996).

[51] R. K. Chang and A. J. Campillo, Eds., "*Optical Processes in Microcavities*," (World Scientific, Singapore, 1996).

[52] P. W. Milloni and P. L. Knight, "Spontaneous emission between mirrors," Opt. Commun. **9**, 119 - 122 (1973).

[53] F. De Martini, G. Innocenti, G. R. Jacobowitz, and P. Mataloni, "Anomalous Spontaneous Emission Time in a Microscopic Optical Cavity," Phys. Rev. Lett. **59**, 2955 - 2958 (1987).

[54] Y. Yamamoto, S. Machida, K. Igeta, G. Bjork, "Controlled Spontaneous Emission in Microcavity Semiconductor Lasers", in Y. Yamamoto, Ed., *"Coherence, Amplification, and Quantum Effects in Semiconductor Lasers,"* Series in Pure and Applied Optics (Wiley, New York, 1991).

[55] H. Yokoyama, K. Nishi, T. Anan, H. Yamada, S. D. Brorson, and E. P. Ippen, "Enhanced Spontaneous Emission from GaAs quantum Wells in Monolithic Microcavities," Appl. Phys. Lett. **57**, 2814 - 2816 (1990).

[56] G. Björk, S. Machida, Y. Yamamoto, and K. Igeta, "Modification of spontaneous emission rate in planar dielectric microstructures, Physical Review A **44**, 669 - 681 (1991).

[57] M. S. Skolnick, T. A. Fisher, and D. M. Whittaker, "Strong Coupling Phenomena in Quantum Microcavity Structures," Semiconductor Science and Technology **13**, 645 - 669 (1998).

[58] Y. Zhu, J. Gauthier, S. E. Morin, Q. Wu, H.J. Carmichael, and T.W. Mossberg, "Vacuum Rabi splitting as a feature of linear dispersion theory: analysis and experimental observations," Phys Rev. Lett. **64**, 2499 - 2502 (1990).

[59] C. Weisbuch, M. Nishioka, A. Ishikawa, and Y. Arakawa, "Observation of coupled exciton-photon mode splitting in a semiconductor quantum microcavity," Phys. Rev. Lett. **69**, 3314 - 3317 (1992).

[60] S. Pau, G. Björk, J. Jacobson, H. Cao, and Y. Yamamoto, "Microcavity exciton-polariton splitting in the linear regime," Physical Review B **51**, 14437 - 14447 (1995).

[61] F. De Martini, G. Innocenti, G.R Jacobovitz and P. Mataloni, "Anomalous Spontaneous Emission Time in a Microscopic Optical Cavity", Physical Review Letters **59**, 2955 (1987).

[62] E. M. Purcell, "Spontaneous Emission Probabilities at Radio Frequencies", Physical Review **69**, 681 (1946).

[63] K. Tanaka, T. Nakamura, W. Takamatsu, M. Yamanishi, Y. Lee and T. Ishihara, Cavity Induced Changes of Spontaneous Emission Lifetime in One-Dimensional Semiconductor Microcavities", Physical Review Letters **74**, 3380 (1995).

[64] F. Tassone, C. Piermarocchi, V. Savona, and A. Quattropani, "Photoluminescence Decay Times in Strong coupling Semiconductor Microcavities" Physical Review B **53**, R7642 (1996).

[65] Y. Yamamoto, S. Machida, and G. Bjork, "Microcavity Semiconductor Laser with Enhanced Spontaneous Emission", Physical Review A **44**, 657 (1991).

[66] D. G. Lidzey, D. D. C. Bradley, S. J. Martin, and M. A. Pate, "Pixelated multicolor microcavity displays," IEEE Journal on Selected Topics in Quantum Electronics **4**, 113 (1998).

[67] H. Yokoyama and K. Ujihara, Eds., "Spontaneous emission and laser oscillation in microcavities," (CRC Press, Boca Raton, 1995).

[68] Y. Yamamoto, F. Tassone, and H. Cao, "*Semiconductor Cavity Quantum Electrodynamics*," Springer Tracts in Modern Physics Series, Vol. 169, (Springer-Verlag, New York, 2000) pp. 1-164.

[69] M. S. Ünlü and S. Strite, "Resonant Cavity Enhanced Photonic Devices," J. Appl. Phys. **78**, 607 (1995).

[70] H. Benisty, H. De Neve, and C. Weisbuch, "Impact of Planar Microcavity Effects on Light Extraction - Part I: Basic Concepts and Analytical Trends," IEEE Journal on Selected Topics in Quantum Electronics **34**, 1612 (1998).

[71] H. Benisty, H. De Neve, and C. Weisbuch, "Impact of Planar Microcavity Effects on Light Extraction - Part II: Selected Exact Simulations and Role of Photon Recycling," IEEE Journal on Selected Topics in Quantum Electronics **34**, 1632 (1998).

[72] R. E. Slusher and C. Weisbuch, "Optical microcavities in condensed matter systems," Solid State Communications **92**, 149 (1994).

[73] H. Yokoyama, K. Nishi, T. Anan, Y. Nambu, S. D. Brorson, E. P. Ippen, and M. Suzuki, "Controlling spontaneous emission and threshold-less laser oscillation with optical microcavities," Optical and Quantum Electronics **24**, S245 (1992).

[74] Y. Yamamoto, S. Machida, and G. Björk, "Microcavity semiconductor laser with enhanced spontaneous emission," Phys. Rev. A **44**, 657 (1991).

[75] J.V. Sandusky and S. R. J. Brueck, "Observation of spontaneous emission microcavity effects in an external-cavity surface emitting laser structure," Applied Physics Letters **69**, 3993 (1996).

[76] S. L. McCall, A. F. J. Levi, R. E. Slusher, S. J. Pearton, and R. A. Logan, "Whispering Gallery Mode Microdisk Lasers," Applied Physics Letters **60**, 289 (1992).

[77] J. P. Zhang, D. Y. Chu, S. L. Wu, S. T. Ho, W. G. Bi, C. W. Tu, and R. C. Tiberio, "Photonic Wire Laser," Physical Review Letters **75**, 2678 (1995).

[78] E. F. Schubert, Y.-H. Wang, A. Y. Cho, l. W. Tu, and G. J. Zydzik, "Resonant Cavity Light Emitting Diode," Applied Physics Letters **60**, 921 (1992).

[79] A.E. Siegman, "Lasers", (University Science Books, 1986).

[80] E. Yablonovitch, "Inhibited spontaneous emission in solid-state physics and electronics," Phys. Rev. Lett. **58**, 2059-2062, 1987.

[81] S. John, "Strong localization of photons in certain disordered dielectric superlattices," Phys. Rev. Lett. **58**, 2486-2489, 1987.

[82] J. D. Joannopoulos, R. D. Meade, and J. N. Winn, "*Photonic Crystals*," (Princeton University Press, New Jersey, 1995) pp. 1-129.

[83] J. D. Joannopoulos, P. R. Villeneuve, and S. H. Fan, "Photonic crystals: putting a new twist on light," Nature **386**, 143-149, 1997.

[84] S. G. Johnson and J. D. Joannopoulos, "*Photonic Crystals: The Road from Theory to Practice*," (Kluwer, Boston, 2002) pp.1-160.

[85] C.M. Soukoulis, "*Photonic Crystals & Light Localization in the 21st Century*," NATO Science Series: C (Kluwer, Norwell, 2001) pp. 1-605.

[86] N. W. Ashcroft and N. D. Mermin, "*Solid State Physics,*" (Saunders College, Philadelphia, Pennsylvania, 1976).

[87] L. Levi, *"Applied Optics: A Guide to Optical System Design,"* Vol. 2, (Wiley, New York, 1980) pp. 47-67.

[88] G. Bjork and O. Nilsson, "A New Exact and Efficient Numerical Matrix Theory of Complicated Laser Structures: Properties of Asymmetric Phase Shifted DFB Lasers," IEEE Journal of Lightwave Technology **5**, 140 (1987).

[89] M. Born and E. Wolf, *"Principles of Optics"* (Cambridge University Press, Cambridge, 1998), pp. 51.

[90] M. Bass, E. W. Stryland, D. R. Williams, and W. L. Wolfe, Eds., *"Handbook of Optics"*, (McGraw-Hill, New York, 1995), pp. 38-42.

4. Design and Fabrication

Hydrogenated amorphous silicon oxide (a-SiO_x:H) passive based Fabry-Perot microcavities based on standard complementary metal oxide semiconductor (CMOS) technology have already been applied to the spectral analysis [91]. The advantage of these optoelectronic microdevices is that they use the well established CMOS electronic integrated circuit (IC) technology. In this research, we have used hydrogenated amorphous silicon oxide (a-SiN_x:H) active microcavities. The microcavity was either realized with metallic or dielectric mirrors.

4.1. Metallic microcavity fabricated without ammonia

The metallic microcavity fabricated without ammonia (NH_3) had a Au back mirror and an a-SiN_x:H-air interface front mirror. First, the thin glass substrates were coated with a 100 nm of Au to fabricate the high reflectance back mirror. Second, a thin layer of a-SiN_x:H was deposited on the Au coated substrates by PECVD. The flow rate of the PECVD gas (2% SiH_4 in N_2) was 180 sccm, the radio frequency (RF) power 10 W, and the deposition chamber pressure 1 Torr. The metric thickness (L) of the a-SiN_x:H layer grown without NH_3 was measured to be 1400 ± 100 nm.

4.2. Metallic microcavity fabricated with ammonia

The metallic microcavity fabricated with NH_3 had an Al back mirror and an a-SiN_x:H-air interface (or a a-SiN_x:H-Al partially transmitting) front mirror. First, the thin Si or quartz substrates were coated with 100 nm of Al in order to fabricate the high reflectance Al back mirror. Second, a thin layer of a-SiN_x:H was deposited on the Al coated substrates by PECVD. The flow rates of the PECVD gases were 180 sccm for 2% SiH_4 in N_2 and 10 sccm for NH_3, the RF power 10 W, and the deposition chamber pressure 1 Torr. The metric thickness (L) of the a-SiN_x:H layer grown with NH_3 was measured to be 1000 ± 100 nm. Finally, the samples were annealed in a forming gas atmosphere at 600°C for 10 min. For the Al partially transmitting front mirror microcavities, a thin (approximately 10 nm) layer of Al was deposited on the annealed samples.

4.3. Dielectric Microcavity fabricated without ammonia

The dielectric microcavity was realized by a $\lambda/2$ active layer of a-SiN_x:H sandwiched between two passive DBR's. First, the bottom DBR was deposited by PECVD on the silicon substrate using $\lambda/4$ alternating layers of a-SiN_x:H (with refractive index = 1.72 and metric thickness = 104±5 nm) and a-SiO_x:H (with refractive index = 1.45 and metric thickness = 124±6 nm). For the nitrogen rich a-SiN_x:H deposition, ammonia (NH_3) with a flow rate of 10 sccm, and 2% silane (SiH_4) in nitrogen (N_2) with a flow rate of 180 sccm were used. For the a-SiO_x:H deposition, nitrous oxide (N_2O) with a flow rate of 25 sccm, and 2% SiH_4 in N_2 with a flow rate of 180 sccm were used. After the deposition of the bottom DBR, a λ/2 layer of silicon rich a-SiN$_x$:H (with refractive index = 2.03 and metric thickness = 163±8 nm) was deposited. For the silicon rich a-SiN$_x$:H deposition, only 2% SiH_4 in N_2 with a flow rate of 180 sccm was used. Afterwards, the top DBR was deposited, using λ/4 alternating layers of a-SiO$_x$:H and a-SiN$_x$:H. The radio frequency (RF) power was 20 W, and the deposition chamber pressure 1 Torr during the continuous deposition process. The m = 1 cavity mode was tuned to the corresponding wavelength and growing the layers accordingly. The PL spectrum of bulk amorphous silicon has an maximum emission at 710 nm. This yields geometrical layer thicknesses of 164 nm and 328 nm for the half wavelength and full wavelength hydrogenated amorphous silicon active layers, respectively, and 123 nm and 104 nm for the silicon oxide and silicon nitride DBR layers, respectively.

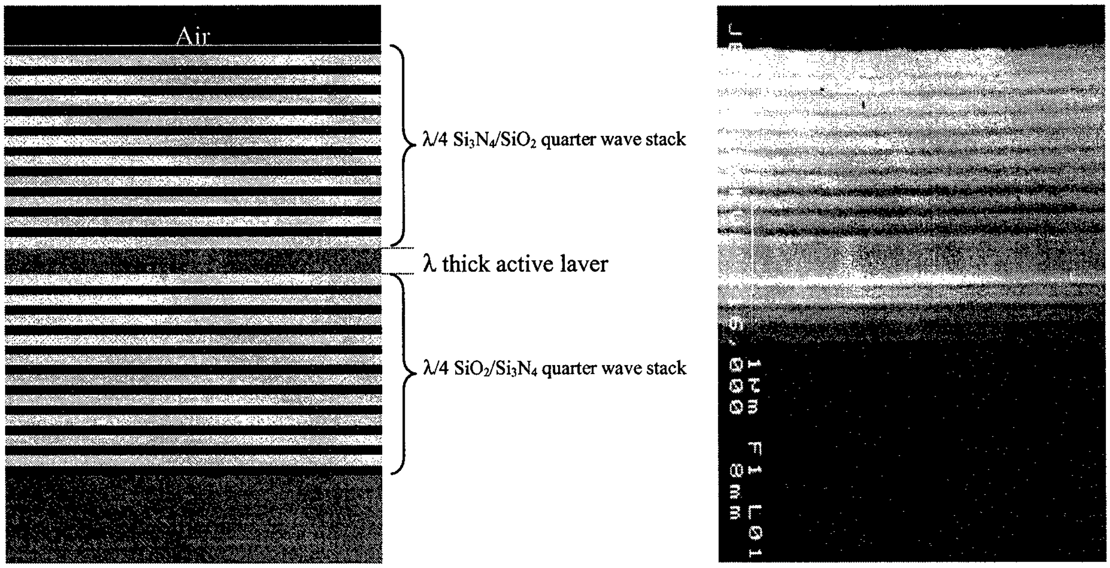

Figure 4.1. The planar microcavity structure with DBR mirrors.

The schematic and the scanning electron microscope (SEM) picture of one of the microcavity structures is shown in the preceding figure. The 328 nm thick a-SiN$_x$:H layer can be distinguished in the middle, although it is mixed up a little with the silicon oxide layers enclosing it. The dark regions are 104 nm thick silicon nitride layers, and the light gray regions are 123 nm thick silicon oxide layers.

4.4. Sample Cleavage, Cleaning and Cleanliness

In the field of device physics cleaning means to remove the undesired materials from the wafer before each process step. The dirt may come either from the surroundings or from the previous process steps. Cleanliness is to prevent the contamination and to maintain the level of cleanliness that is already present. These two definitions are in fact very simple, but they are very crucial for achieving high performances in the production of semiconductor devices.

Clean rooms are categorized by the number of particles contained in the air. A clean room categorized as a class-100 clean room has 100 or less particles that are 0.5 micrometer or greater in diameter, in a cubic foot of air. A class-100, which is used for fabrication of semiconductor devices, requires good filtering techniques and protective clothing on personnel. Class-10000, which is relatively easy to obtain, is generally used for semiconductor characterization. For comparison, the general environment of an average building usually exceeds class-100000.

Because we fabricate our devices in just one step by PECVD, cleaning operation is performed once, after cleaving. The wafers are cleaved into pieces of dimensions 2.0 x 2.0 cm^2 to fit them into our reflectance measurement setup. This size is also big enough to assume in theoretical calculations, that the cavity has infinite dimensions in the x -y plane. In our processes, we performed 3-solvent cleaning, in which the solvents are Tricholoroethan (TCE), Aceton (ACE), and Isopropyl Alcohol (ISO). The samples were boiled for 2 minutes in TCE, and then left at room temperature and then rinsed with deionized water. Drying is very important such that no droplets should be evaporated on the surface, since they carry dirt. For this reason nitrogen gun is used for removing the water from the surface. Finally the samples are kept on the hot plate at 120°C for 50 seconds. The solvents are semiconductor grade, that is they are extremely pure and filtered in sub-microns. Organic solvents are effective in removing oils, greases, waxes and organic materials. Many cleaning methods with various materials procedures do exist, and they are chosen by trial and error.

4.5. Plasma Enhanced Chemical Vapor Deposition

Plasma processing is used extensively in the semiconductor industry for etching and growth of thin film materials [92]. Plasma assisted techniques are especially important in deposition of thin-film materials because they can be accomplished at relatively low temperatures. Such materials could be deposited on wafers using chemical vapor deposition, in which the reactant species are introduced into the vicinity of a hot wafer by gaseous flow and the appropriate reactions to drive this chemical reactions are often 700° to 1000° C. For gallium arsenide wafers, arsenic evolves in this temperature range. Metals commonly present on the wafer can not be exposed to these extremes either. As one example ohmic constants are formed at approximately 450° C. Temperatures above 500° C will rapidly destroy the ohmic contact. Therefore CVD is not a generally useful technique, so low-temperature, plasma driven reactions are used instead. The plasma-assisted deposition process is denoted as plasma-enhanced chemical vapor deposition (PECVD). PECVD yields films that are amorphous in nature with very little short range structural ordering. Chemical bonding within the film may vary. The plasma assisted deposition process sometimes has been called plasma polymerization to emphasize that the film may be randomly bonded, and highly cross-linked. Therefore, chemical species other than the desired ones are often included in the film. In this sense, plasma assisted deposition is more complex than plasma-assisted etching, in which it does not much matter what the final products are, because they disappear into the pumps.

From the perspective of a physicist, the plasma state encompasses a wide range of electron energies and densities and includes such phenomena as flames, low-pressure arcs, solar coronas, and thermonuclear reactions. The regime of interest to semiconductor processing is the low-pressure plasma or glow discharge regime. These plasmas are characterized by gas pressures on the order of 0.1 to several Torr, free-electron densities of 10^9 to 10^{12} cm^{-3}, and electron energies of 1.0 to 10.0 e V.

The plasma is able to generate chemically reactive species at relatively low temperature because of the nature of the plasma state. The temperature of the chemical species (atoms, molecules, or radicals), as represented by their translational and rotational energy, is generally near ambient. The electrons, however, can exhibit temperatures of tens of thousands of degrees Kelvin. The electron energy is sufficient to break molecular bonds and create chemically active species in the plasma. Any of these species can be excited to higher electronic energy states by further interaction with the electrons. Hence, chemical reactions that usually occur only at high temperatures can be made to occur at low or even ambient temperatures in the presence of an activating plasma state. Most of the species remain neutral in glow discharges. This feature allows most of the plasma to remain near ambient temperatures. Although the ionization rate is small, it is adequate to provide sufficient number of reactive species. The light glow emitted from the plasma is characteristic of the electronic transitions taking place. The wafer is generally heated to aid the deposition process, but usually less than a few hundred degrees Celsius.

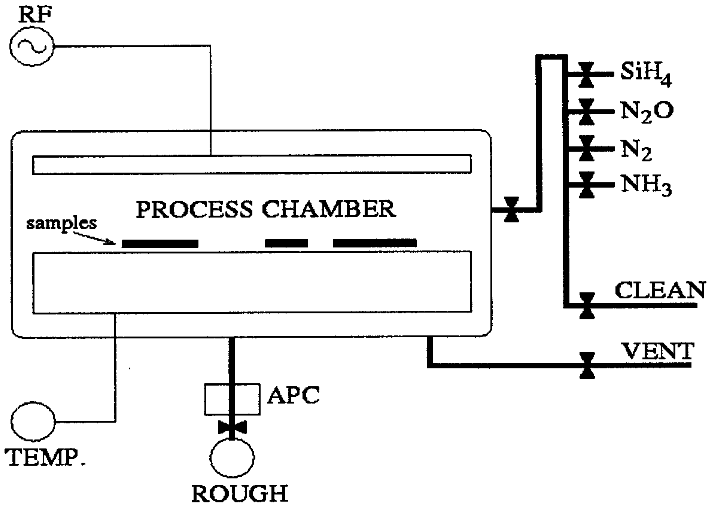

Figure 4.2. The schematic of the Plasma Enhanced Chemical Vapor Deposition (PECVD) system.

Plasma processing occurs in equipment called plasma reactors. Wafers are placed on the lower electrode, which is also used to heat wafers. The 13.56 MHz RF signal which excites the plasma is applied across the two electrodes. The reactant gases are introduced at the outer radius, and flow radially between the electrodes. The plasma occupies the region between the two electrodes, but is excluded from the immediate vicinity of the electrode surface by electromagnetic effects. This region is called the plasma sheath or the dark region (because it doesn't glow). It is on the order of 0.1 to 10.0 mm thick, depending on the operating conditions. The plasma is generally neutral, with positive species balancing negative ones. However, the plasma sheath is a region of positive space charge and the electrode surfaces are negative with respect to the plasma. This is due to the higher mobility of electrons, which move rapidly to the surface of electrodes. The RF voltage is applied through a large blocking capacitor, so that no dc bias is intentionally applied. Most of the voltage between the two electrodes is dropped across the two plasma sheaths.

The plethora of chemical species in the plasma and the nature of the plasma state make processing results extremely sensitive to virtually all possible parameters: gas type, gas flow rate, gas delivery position, pressure, electrode geometry, power, power density, radio frequency, wafer temperature, and wafer material The possible chemical reactions can be highly complex, because of the presence of so many radicals. These considerations mean that plasma processes are developed more by empirical means than by theoretical analysis.

A number of materials have been grown by using PECVD. The major materials are hydrogenated amorphous silicon nitride ($n = 1.7$) and hydrogenated amorphous silicon oxide ($n = 1.4$) are used particularly for inter-level dielectrics, capacitor dielectrics, and scratch protection. They are used as the alternating refractive index layers of the DBR's.

4.6. Nitrogen rich hydrogenated amorphous silicon nitride deposition

A mixture of 2% silane (SiH_4) and 98% nitrogen (N_2) is used as the silicon source, and ammonia (NH_3) as the nitrogen source. The desired overall reaction would be

$$3SiH_4 + 4NH_3 \rightarrow Si_3N_4 + 12H_2$$

or

$$3SiH_4 + 2N_2 \rightarrow Si_3N_4 + 6H_2$$

but there are enormous number of possible intermediate reactions. Oxygen may be present from background gases or water Carbon may be present from background hydrocarbons, such as pump oil. The resulting "silicon nitride" may include Si, N, 0, H, and C. Even in the complete absence of background components or contamination, hydrogen will be included in the film because of ammonia. In fact, plasma a-SiN_x:H can contain as much as 20-25% hydrogen. [93-94] So the Si/N ratio will not necessarily be 3/4, it is a function of the operating parameters.

Parameter	Value
Automatic Pressure Controller (APC) Pressure	1000 m Torr
RF Power	20 W
Temperature	100°C
2%SiH_4+98%N_2 Flow Rate	180 sccm
NH_3 Flow Rate	10 sccm
Process Time	5.60 minutes

Table 4.1. Nitrogen rich hydrogenated amorphous silicon nitride PECVD recipe

The recipe in the previous table was found by empirical means and used, to deposit approximately 1040 Å thick nitrogen rich hydrogenated amorphous silicon nitride (a-SiN_x:H) layer.

4.7. Hydrogenated amorphous silicon oxide deposition

Although it is common to refer to plasma deposited hydrogenated amorphous silicon oxide (a-SiO_x:H) as "silicon dioxide", the same caveats on stoichiometry, that applied to a-SiN_x:H, also apply here. The Si/O ratio may depart from ½. The mixture of 2% silane (SiH_4) and 98% nitrogen (N_2) is used as the silicon source , and nitrous oxide (N_2O) as the oxygen source. The desired overall reaction would be

$$SiH_4 + 2N_2O \rightarrow Si0_2 + 2N_2 + 2H_2$$

Oxygen has a much greater affinity for reacting with silane than does nitrogen. Hence, silicon oxide formation dominates over silicon nitride formation. The recipe in the below table was used to deposit approximately 1230 Å thick layer.

Parameter	Value
Automatic Pressure Controller (APC) Pressure	1000 m Torr
RF Power	20W
Temperature	100°C
2% SiH_4 + 98% N_2 Flow Rate	180 sccm
N_2O Flow Rate	25 sccm
Process Time	2.81 minutes

Table 4.2. Hydrogenated amorphous silicon oxide PECVD recipe

The thickness and the refractive indices of a-SiO_x:H and a-SiN_x:H layers were measured by an ellipsometer. Although the precision of the ellipsometer is 1 Angstrom (Å), subsequent measurements may differ, e.g., about 10 - 20 Å for 1230 Å thick a-SiO_x:H layer, which means an error of approximately 1.5%.

4.8. Silicon rich hydrogenated amorphous silicon nitride deposition

Hydrogen is included in the plasma deposited film, because silane is used as the silicon source. Like a-SiN_x:H and a-SiO_x:H, although we refer to our plasma deposited material as "hydrogenated amorphous silicon", it contain N, because silane is mixed with a carrier gas, N_2. Oxygen may be present from background gases or water, carbon may be present from background hydrocarbons. So the resulting "hydrogenated amorphous silicon" includes Si, H, N, 0, and C. The recipe used to deposit approximately 1640 Å thick hydrogenated amorphous silicon nitride layer is given in the below table. Ellipsometer can not measure the thickness and the refractive index of amorphous silicon. The thickness was measured by a surface texture analysis system to be 1640 ± 30 Å and the refractive index was estimated from the literature to be 2.18. [95, 96]

Parameter	**Value**
Automatic Pressure Controller (APC) Pressure	1000 m Torr
RF Power	20 W
Temperature	100°C
2% SiH_4 + 98% N_2 Flow Rate	180 sccm
Process Time	6.34 minutes

Table 4.3. Silicon rich hydrogenated amorphous silicon nitride PECVD recipe

4.9. References

[91] J. H. G. Correia, "Optical Microsystems in Silicon Based on a Fabry-Perot Resonance Cavity, Application for Spectral Analysis of Visible Light," (Delft University Press, Delft, 1999) pp. 1-196.

[92] R. Williams, "Modern GaAs Processing Methods", (Artech House, Boston, 1990) pp. 153.

[93] W. A. Lanford, and M. J. Rand, J. Appl. Phys. **49**, 2473 (1978).

[94] A. Aydinli, A. Serpengüzel and D. Vardar, "Visible Photoluminescence from Low Temperature Deposited Hydrogenated Amorphous Silicon Nitride", Solid State Commun. **98**, 4 (1996).

[95] A. Serpengüzel, A. Aydinli, and Alpan Bek, "Enhancement and Inhibition of Photoluminescence in Hydrogenated Amorphous Silicon Nitride Microcavities", Opt. Express **1**, 108 (1997).

[96] A. Serpengüzel, A. Aydinli, and Alpan Bek, "Alteration of Spontaneous Emission in hydrogenated Amorphous Silicon Microcavities", J. Non-Crystalline Solids, **227-230**, 1142-1145 (1998).

5. Characterization and Results

5.1. Photoluminescence measurements

Photoluminescence (PL) study of a sample is a good technique to characterize the material, revealing the optical characteristics of the sample. To investigate the light emission properties of the sample, a PL spectrum is necessary. This analysis helps in understanding the energy band structure of the sample, therefore determining the emission wavelength, together with some other material parameters. The interaction of light with semiconductors occur at the spectral range 0.1-1000 μm (0.001-12 eV). In the near ultraviolet, visible, near infrared region (0.24-3.1 eV) the dominant effect is absorption at the band gap and by impurities, leading to PL under certain conditions.

A valence electron can be excited across the band gap of a semiconductor with an incoming photon, whose energy equals to or exceeds the gap value. Absorption also occurs, when the photon raises an electron from a neutral donor level to the conduction band, or from the valence band to a neutral acceptor level. It is also possible to induce absorptive transition from the valence band to an ionized donor level, or from an ionized acceptor level to the conduction band. These processes lead to the sensitive probe of PL, which occurs when the excited electron returns to its initial state. This process can be either radiative or non-radiative. If it is radiative, it emits a photon whose energy gives the difference between the excited and the initial state energies. The emission spectrum shows a fingerprint peak related to the energy of each excited level.

The gap being direct or indirect strongly affects the absorption process. The incoming photon carries negligible momentum compared to that of the electron, so the absorbing electron gains energy without changing its wavevector. In a direct gap semiconductor like GaAs an electron at the valence band maximum, executes a vertical transition to the conduction band minimum directly above. From the energy conservation,

$$h\nu = Ef - Ei,$$

where Ef and Ei are the final and initial energies of the electron, and hν is the photon energy.

For an indirect gap semiconductor like crystalline silicon, the excited electron needs additional momentum to reach the conduction band minimum at a nonzero wavevector. It gains this momentum through a phonon,

$$h\nu = Ef - Ei \pm h\Omega,$$

where hΩ is the phonon energy, and ± corresponds to the phonon emission and absorption. Phonon emission dominates at low temperatures, since there are less phonons. The need for an additional third body interaction with the phonon makes indirect absorption far less probable then direct absorption, resulting in a weak absorption.

After any of the absorption processes separates an electron and a hole, they recombine. This can proceed in either radiative or non-radiative form. In a direct gap semiconductor, the recombination transition is vertical. For an indirect gap, a phonon must be involved as in indirect absorption. Because of the same reason, as in absorption, the indirect recombination process is much less probable than direct recombination. This explains why crystalline silicon, with its indirect band gap, is a poor light emitter.

Although radiative emission is in many ways the inverse of absorption, there are two main distinctions. One is that recombination is a non-equilibrium process, requiring a supply of electrons at energies above their equilibrium values. For this reason lasers are used as pumping sources. Second, all electronic states whose energy difference obey the conservation law participate in absorption, leading to broad spectral features. But for emission, the recombining electron hole pairs have well defined energy levels, resulting in narrow spectral features. This is why PL is a better tool for characterization than absorption spectroscopy. The sharp peaks of PL can yield highly accurate values for the gap and impurity energies.

The room temperature PL setup consists of a pump laser, a spectrometer, a lock-in amplifier, and a digital oscilloscope. The collected PL signal is imaged to the entrance slit of the spectrometer, whose output is fed to a sensitive photomultiplier tube (PMT). A lock-in-amplifier is providing the necessary electronic gain to the PMT output gain in phase with the laser pulse. The digital oscilloscope is used for monitoring and optimizing the PMT signal. All of the measurement and test devices are computer controlled and the data is acquired digitally. For the room temperature measurements at 300 K the samples are attached to a holder. For low temperature measurements the samples are placed in a closed cycle cryostat system. The closed cycle cryostat system is used to control the sample temperature from 10 K to 300 K.

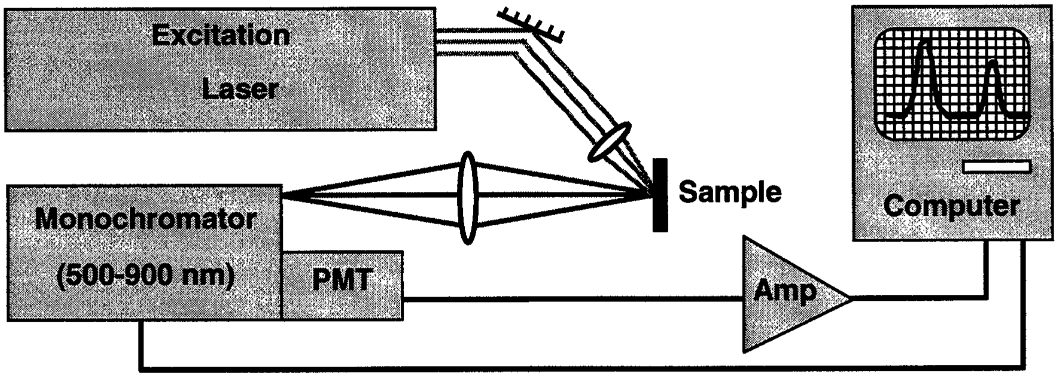

Figure 5.1. The experimental photoluminescence setup.

5.2. Transmittance, reflectance, and absorbance measurements

The visible-near-infrared spectrophotometer is used for the transmittance, reflectance, and absorbance (TRA) measurements of bulk and microcavity sample. The optical design of the spectrophotometer is shown in the following figure. [97] The light from the source, which passes through the filter wheel is directed through the entrance slit into the monochromator, where the grating disperses the light into its monochromatic components. After passing through the monochromator, the light is split into two equal beams. One of the beams is directed onto the sample at 0° with respect to the surface normal and reflected, the other is used as reference beam to compensate the spectrum obtained for changes in some of the system variables. The beams are then recombined and enter the detector compartment. Reflected intensity is calibrated relative to a "perfect reflector," which was an aluminum mirror.

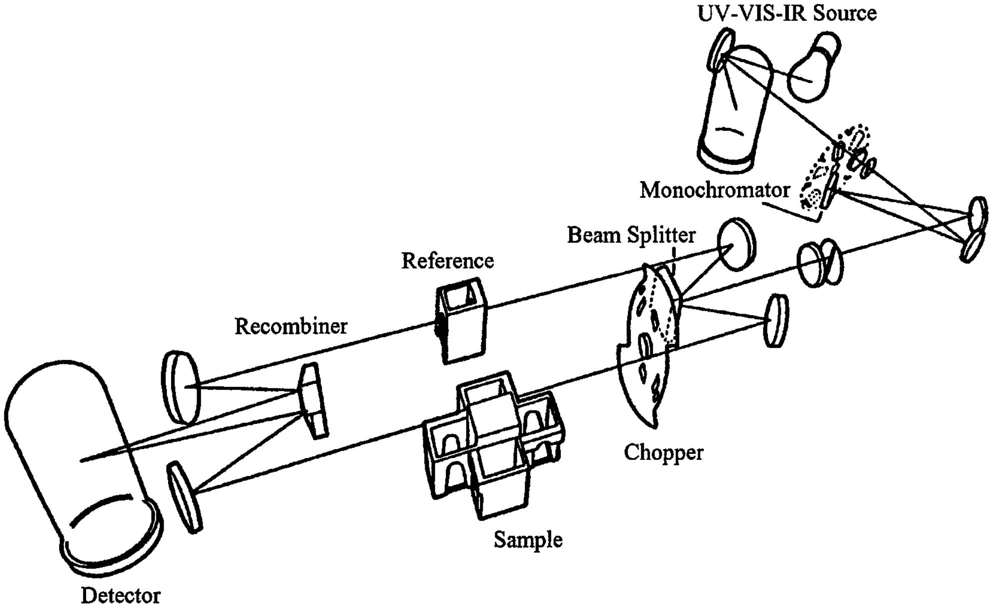

Figure 5.2. Layout of the spectrophotometer.

5.3. Temperature dependence of the PL

The following figure shows the PL spectra of the a-SiN$_x$:H measured in the 550 - 900 nm wavelength and in the 12 – 298 K temperature range at a constant excitation laser intensity of 0.1 W cm^{-2}. A broad PL band centered at 710 nm (E_p = 1.746 eV) at 12 K is observed. The PL spectra have approximately a Gaussian lineshape modulated slightly by Fabry-Perot resonances. These resonances are due to the Fresnel reflections from the a-SiN$_x$:H film surfaces. The PL intensity decreases with increasing temperature. This feature is typical of the PL, which is due to donor-acceptor pair transitions observed in semiconductors [98].

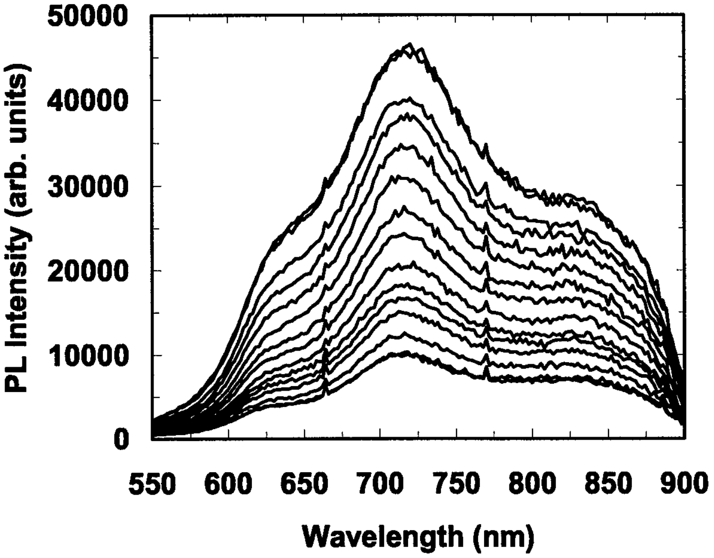

Figure 5.3. PL spectra of a-SiNx:H in the 12 - 298 K temperature range.

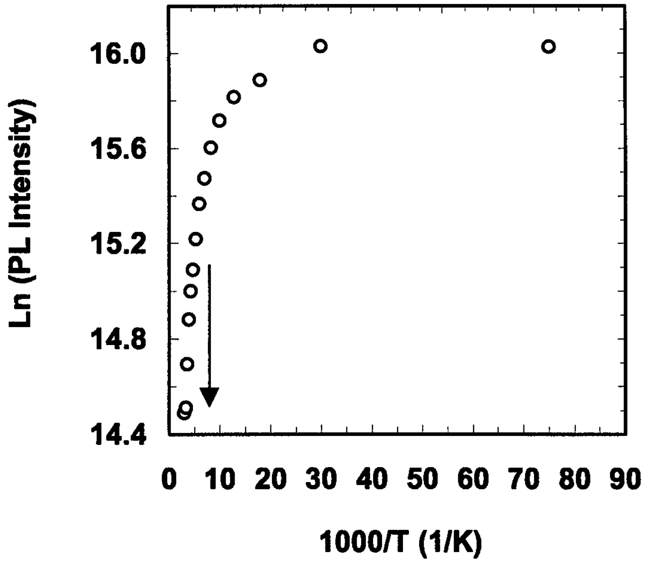

Figure 5.4. Temperature dependence of a-SiN$_x$:H PL intensity at the emission band maximum. The arrow at 170 K shows the starting point of the intensive quenching.

The variation of the PL peak with respect to temperature is plotted in the previous figure. In the 12 - 170 K range, the PL intensity decreases slowly. Above 170 K, however, the PL intensity decreases at a larger rate due to a thermal quenching process. The activation energy ΔE for this thermal quenching process can be derived in the 170 - 298 K temperature range using a nonlinear least squares fit to the following equation,

$$I = I_o \exp(\Delta E/k_B T),$$

where I is the PL intensity, I_o a proportionality constant, and k_B the Boltzmann's constant. The semilog plot of the emission band intensity as a function of the reciprocal temperature gives a straight line in the 170 - 298 K region. An activation energy of $E_a = 0.027$ eV for the emission band is derived from the slope of the straight line fit. This activation energy is associated with a shallow level located at 0.027 eV from the band. This shallow level in undoped a-SiN$_x$:H may be associated with the presence of defects and unintentional impurities [99].

5.4. Power dependence of the PL

The following figure presents the PL spectra for 10 different laser intensities at 12 K. As the power is increased the PL intensity increases.

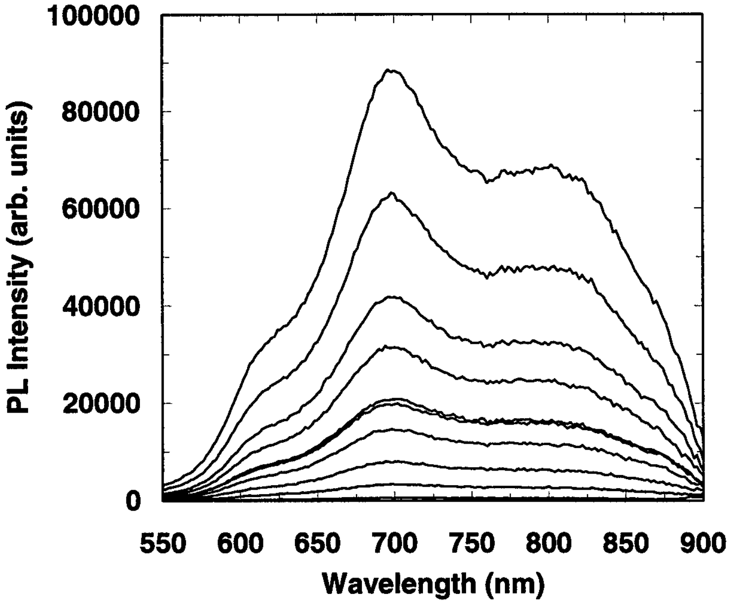

Figure 5.5. PL spectra of a-SiN$_x$:H in the 0.1 – 3.7 W cm^{-2} laser intensity range at 12 K.

The intensity variation of the emission band versus the excitation laser intensity at T = 12 K is also investigated and plotted in the following figure. The experimental data can be fitted by a simple power law,

$$I \propto L^{\gamma},$$

where I is the PL intensity, L the excitation laser intensity, and γ a dimensionless exponent. It was found that, the PL intensity increases sublinearly (i.e., $\gamma = 0.89$) with respect to the excitation laser intensity. For an excitation laser photon with an energy exceeding the band gap energy E_g , the coefficient γ is generally $1 < \gamma < 2$ for the free- and bound-exciton emission, and $\gamma \leq 1$ for free-to-bound and donor-acceptor pair recombination [100]. Thus, the obtained value of $\gamma = 0.89$ confirms the assignment of the observed emission band in a-SiN$_x$:H is due to donor-acceptor pair recombination.

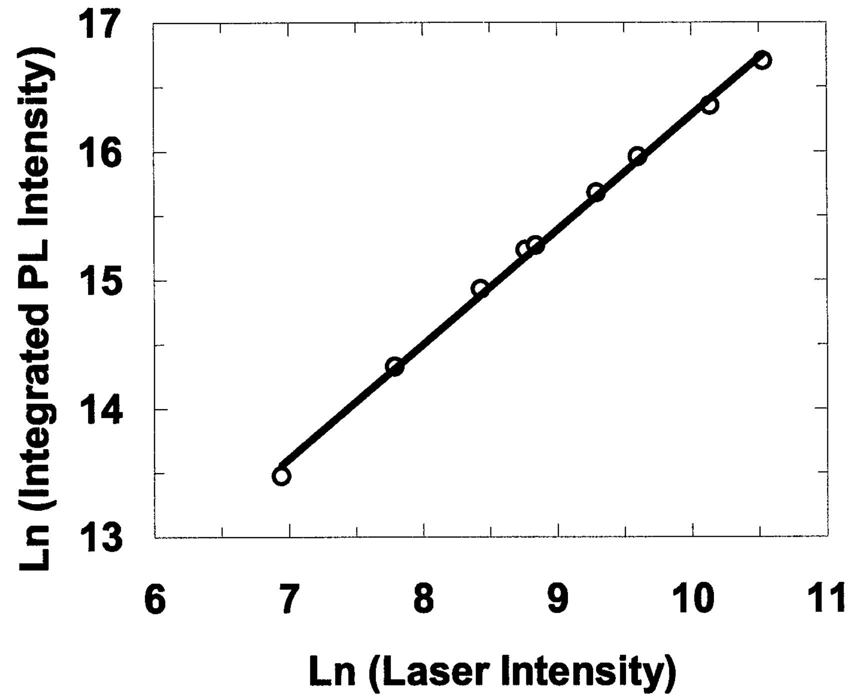

Figure 5.6. Dependence of a-SiN$_x$:H integrated PL intensity versus excitation laser intensity at 12 K. The solid curve gives the theoretical fit using Eq. $I \propto L^{\gamma}$.

5.5. TRA of the a-SiN$_x$:H fabricated without ammonia

The following figure shows the measured and calculated transmittance, (a) reflectance, (b) and absorbance (c) spectra of the bulk a-SiN$_x$:H fabricated without ammonia (NH$_3$). The absorbance spectrum is obtained by subtracting both the reflectance and transmittance spectra from unity, i.e., 100%.

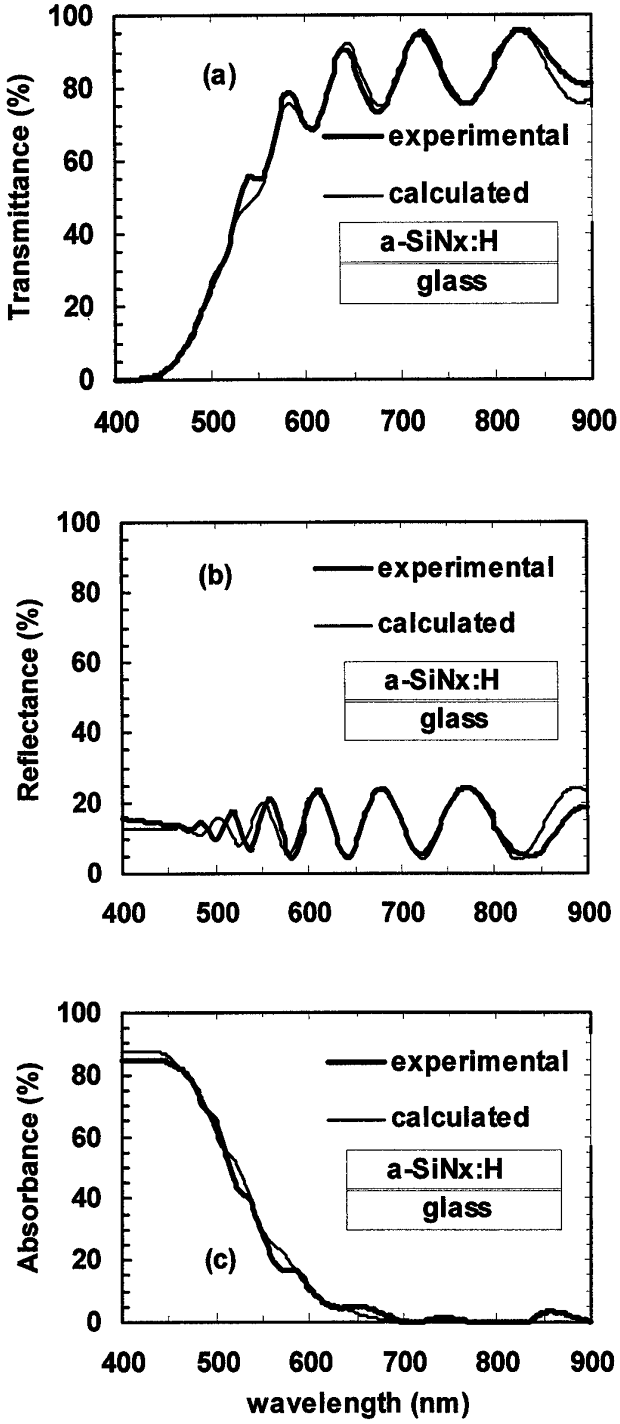

Figure 5.7. Experimental and theoretical (a) transmittance, (b) reflectance, and (c) absorbance spectra of the silicon rich a-SiN$_x$:H fabricated without NH$_3$.

In the calculations, the total transmitted and the reflected electric fields for each wavelength were obtained using an absorbing Fabry-Perot microcavity model. In this model, we assumed the sample to be a one dimensional absorbing dielectric slab. The experimentally measured absorbance spectrum was obtained by subtracting both the experimentally measured transmittance and the reflectance spectra from 100%. This experimentally measured absorbance spectrum was then incorporated to the calculations of the transmitted and reflected electric fields. The calculated transmittance and reflectance at each wavelength were obtained from their respective electric fields. Later, as a final check, the calculated transmittance and reflectance intensity was subtracted from 100% to obtain the calculated absorbance.

The theoretical fit to the experimental spectra is extremely good. The metric thickness of the a-SiN_x:H is found to be L = 1376 nm (which agrees well with the experimental thickness of 1400 ± 100 nm) and the refractive index n = 2.1. Both the transmittance (maxima) and reflectance (minima) spectra show Fabry-Perot resonances at wavelengths (λ_m) satisfying the microcavity resonance condition:

$$\lambda_m = \frac{2Ln}{m}, \tag{1}$$

where m is the quantized mode number, L the metric thickness, and n the refractive index of the microcavity. The microcavity is formed because of the Fresnel reflections from the air and glass interfaces. The mode number of these resonances were found to range from m =11 (λ_{11} = 545 nm) to m = 7 (λ_7 = 835 nm). The resonances have linewidths of $\Delta\lambda$ = 35 nm and quality factors of Q = 20. Below 600 nm, the resonances start to wash out by the absorption of the a-SiNx:H. The loading of the resonances by the a-SiNx:H absorption stops above 600 nm.

5.6. PL of the metallic microcavity fabricated without ammonia

The following figure shows the PL of the metallic a-SiN_x:H microcavity fabricated without NH_3, whose transmittance, reflectance, and absorbance spectra were shown in the previous figure. The PL intensity is modulated by the weak Fabry-Perot resonances, which correlate well with the maxima of the transmittance spectrum, and the minima of the reflectance spectrum. The red-near-IR PL has a broad linewidth (250 nm). This broad linewidth heralds a-SiN_x:H as a novel photonic gain medium.

The Fabry-Perot resonances have experimental and theoretical linewidths of $\Delta\lambda$ = 25 nm and quality factors of Q = 30. The metric thickness of the a-SiN_x:H microcavity with the Au mirror was found to be L = 1438 nm (which agrees well with the experimental thickness of 1400 ± 100 nm) and the refractive index n = 2.1. The PL is modulated by the strong Fabry-Perot resonances. The mode number of these resonances were found to range from m = 11 (λ_{11} = 558 nm) to m = 7 (λ_7 = 874 nm).

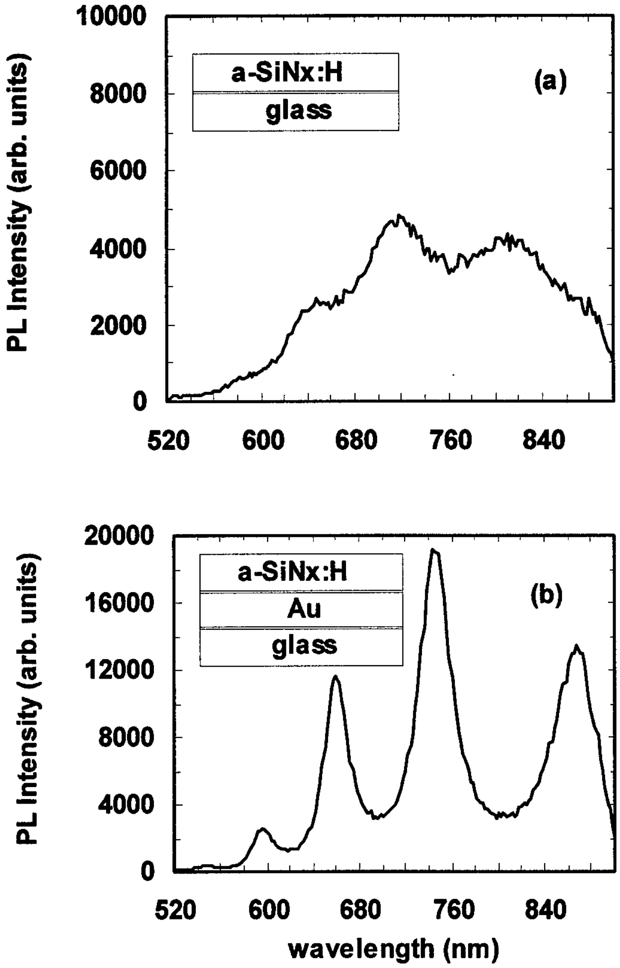

Figure 5.8. PL spectrum of the nitrogen rich a-SiN_x:H microcavity fabricated without NH_3 (a) without the Au back mirror and (b) with the Au back mirror.

The PL spectra of the above figure were obtained under the same experimental conditions. When comparing the spectra, the PL of the microcavity with the Au mirror has 3 noteworthy features with respect to the PL of the bulk a-SiN_x:H : (1) there is a 2X increase of the overall spectrum average (i.e., averaging out the Fabry-Perot resonances), (2) there is a 4X enhancement of the PL peaks, and (3) the PL dips have similar amplitude. These 3 features are noticed with respect to the PL of the bulk a-SiN_x:H. The 2X increase is due to the "round trip" of the excitation laser in the Fabry Perot cavity due to the presence of the back Au mirror. Since the wavelength of the laser is non-resonant, the input laser light does not resonate in the cavity, which would have enhanced the PL further. The 4X enhancement at the resonances, are clearly due to the combined effect of the enhancement of the PL by the cavity resonances with that of the input laser reflecting from the back Au mirror. The PL dips having the same amplitude in both spectra is due to the inhibition of the PL in between the resonances.

5.7. TRA of the bulk a-SiN$_x$:H fabricated with ammonia

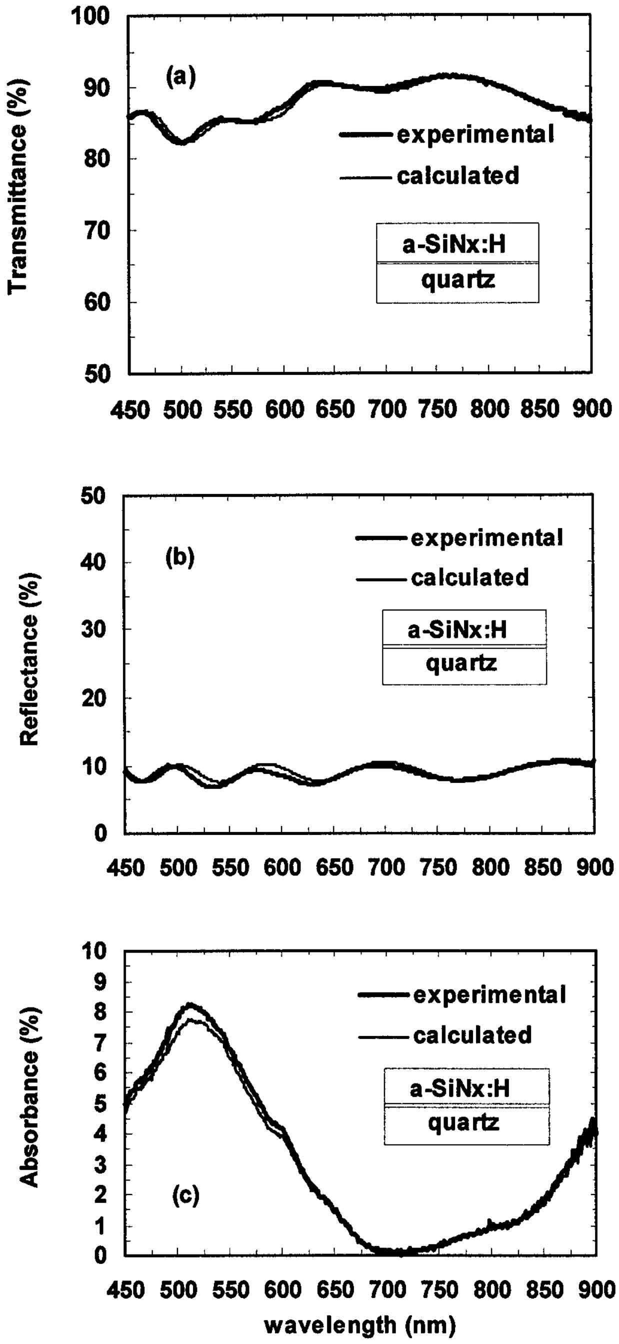

Figure 5.9. Experimental and theoretical (a) transmittance, (b) reflectance, and (c) absorbance spectra of the bulk a-SiN$_x$:H fabricated with NH_3.

The previous figure shows the measured and calculated transmittance, (a) reflectance, (b) and absorbance (c) spectra of the bulk a-SiN_x:H fabricated with NH_3. The absorbance spectrum is obtained by subtracting both the reflectance and transmittance spectra from unity, i.e., 100%. The calculations were performed using the absorbing Fabry-Perot microcavity model described in the previous section.

The theoretical fit to the experimental spectra is extremely good. The metric thickness of the a-SiN_x:H grown with NH_3 is found to be L = 963 nm (which agrees well with the experimental thickness of 1000 ± 100 nm) and the refractive index n = 1.6. Both the transmittance (maxima) and the reflectance (minima) spectra show Fabry-Perot resonances at wavelengths (λ_m) satisfying the microcavity resonance condition. The microcavity is formed by Fresnel reflections from the air and quartz interfaces. The mode number of these resonances were found to range from m =7 (λ_7 = 461 nm) to m = 4 (λ_4 = 760 nm). The resonances have linewidths of $\Delta\lambda$ = 40 nm and quality factors of Q = 10. Compared with the absorption of the a-SiN_x:H grown without NH_3, the absorption of the a-SiN_x:H grown with NH_3 is an order of magnitude lower. Consequently, there is no loading of the resonances by the absorption.

5.8. PL of the metallic microcavity fabricated with ammonia

The following figure shows the PL of the a-SiN_x:H grown with NH_3 on Si together with the samples grown on quartz, whose transmittance, reflectance, and absorbance spectra were shown previously. The samples grown on quartz are used for transmittance and reflectance measurements. The samples grown on Si are used for PL measurements, since Al sticks better to Si when compared with quartz.

The PL intensity is modulated by the weak Fabry-Perot resonances. The mode number of these resonances were found to range from m = 7 (λ_7 = 488 nm) to m = 6 (λ_6 = 572 nm). The PL is inhibited in between these two resonances at m = 6.5 ($\lambda_{6.5}$ = 524 nm). The blue-green PL has also a broad linewidth (100 nm). This broad linewidth again shows that, a-SiN_x:H has potential as a novel photonic gain medium. The Fabry-Perot resonances have experimental and theoretical linewidths of $\Delta\lambda$ = 40 nm and quality factors of Q = 10. The metric thickness of the a-SiN_x:H grown on Si was found to be L = 1103 nm (which agrees well with the experimental thickness of 1000 ± 100 nm) and the refractive index n = 1.6.

Figure (b) depicts the PL of the a-SiN_x:H microcavity with the Al back mirror. Al is chosen instead of Au, because Al has higher reflectance in the blue-green part of the optical spectrum. The Fabry-Perot resonances have experimental and theoretical linewidths of $\Delta\lambda$ = 60 nm and quality factors of Q = 8. The metric thickness of the a-SiN_x:H microcavity with the Al mirror was found to be L = 929 nm (which agrees well with the experimental thickness of 1000 ± 100 nm) and the refractive index n = 1.6. The PL is modulated by the strong Fabry-Perot resonances. The mode number of these resonances were found to range from m = 6 (λ_6 = 515 nm) to m = 5 (λ_5 = 603 nm).

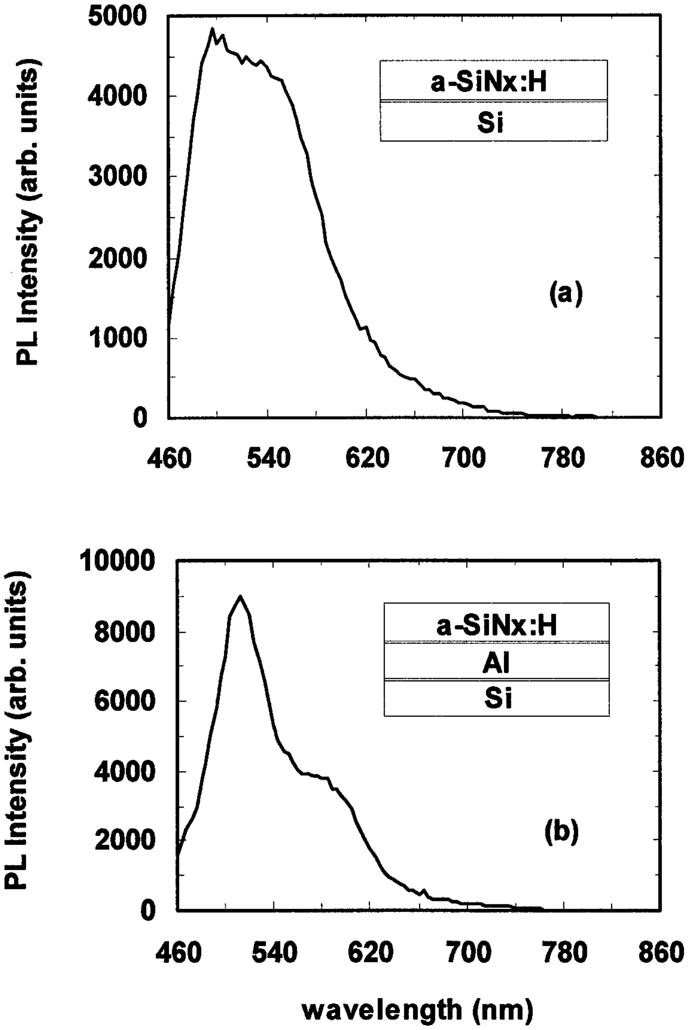

Figure 5.10. PL spectrum of the nitrogen rich a-SiN_x:H metallic microcavity fabricated with NH_3 and (a) without or, (b) with the Al mirror.

The two PL spectra of the above figure were obtained under the same experimental conditions. When comparing the spectra, the PL of the microcavity with the Al mirror has 3 noteworthy features with respect to the PL of the a-SiN_x:H : (1) there is a 1.3X increase of the overall spectrum average (i.e., averaging out the Fabry-Perot resonances), (2) there is a 2X enhancement of the PL peaks, and (3) the PL dips have similar amplitude. These 3 features are noticed with respect to the PL of the a-SiN_x:H. The 1.3X increase is due to the "round trip" of the laser in the cavity due to the presence of the back Al mirror instead of a Si substrate, which only partially reflects the incident beam. Since the wavelength of the laser is non-resonant, the input laser light does not resonate in the cavity, which would have enhanced the PL further. The 2X enhancement at the resonances, are clearly due to the combined effect of the enhancement of the PL by the cavity resonances with that of the input laser reflecting from the back Al mirror. The PL dips having the same amplitude in both spectra is due to the inhibition of the PL in between the resonances.

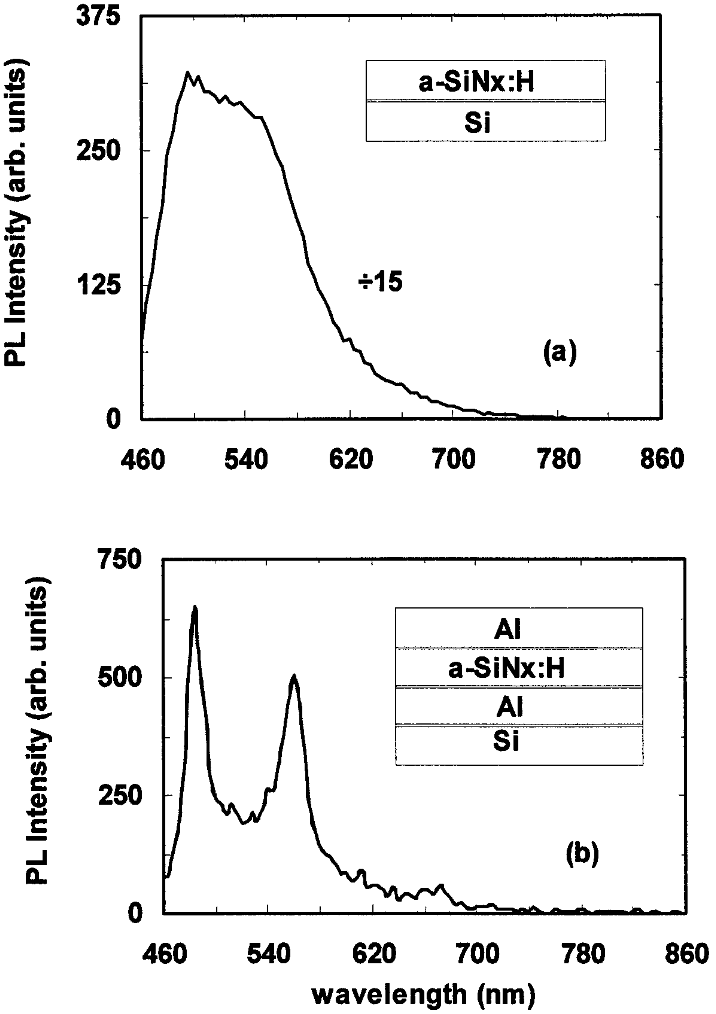

Figure 5.11. PL spectrum of the nitrogen rich a-SiN$_x$:H metallic microcavity fabricated with NH$_3$ and (a) without the Al back mirror, (b) with the Al back and front mirrors.

The above figure shows the PL of the a-SiN$_x$:H grown with NH$_3$ divided by 15, in order to have the same spectral average for both figures. Figure (b) depicts the PL of the a-SiN$_x$:H microcavity with the Al back and Al front partially transmitting mirror. The Fabry-Perot resonances have experimental and theoretical linewidths of $\Delta\lambda$ = 20 nm and quality factors of Q = 25. The metric thickness of the a-SiN$_x$:H microcavity with the Al back and partially transmitting front mirror was found to be L = 1072 nm (which agrees well with the experimental thickness of 1000 ± 100 nm) and the refractive index n = 1.6. The PL is modulated by strong Fabry-Perot resonances. The mode number of these resonances were found to range from m = 7 (λ_7 = 488 nm) to m = 5 (λ_5 = 687 nm). When comparing the spectra in (a) and (b), the PL of the microcavity with the Al back and partially transmitting Al front mirror has 3 noteworthy features with respect to the PL of the a-SiN$_x$:H : (1) the overall spectral averages are the same (i.e., averaging out the Fabry-Perot resonances), (2) there is a 2X enhancement of the PL peaks, and (3) the PL dips have similar amplitude. These 3 features are noticed with respect to the PL of the nitrogen rich a-SiN$_x$:H. The 2X enhancement at the resonances, while the overall average being the same, is clearly due to the enhancement of the PL by the cavity resonances. The PL dips having the same amplitude in both spectra is due to the inhibition of the PL in between the resonances.

5.9. Dielectric silicon rich a-SiN$_x$:H microcavity

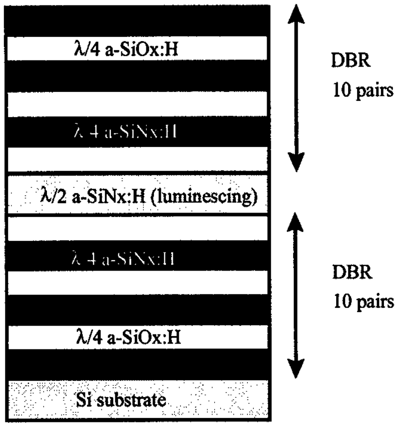

Figure 5.12. The schematic of the dielectric silicon rich a-SiN$_x$:H microcavity.

In this section, we study, the alteration of PL in an all dielectric silicon rich a-SiN$_x$:H microcavity. We also study the measured and calculated reflectance of the all dielectric silicon rich a-SiN$_x$:H microcavity. The previous figure shows a schematic of the dielectric silicon rich a-SiN$_x$:H microcavity. The λ/4 passive nitrogen rich a-SiN$_x$:H layers are shown in black, while the λ/4 passive a-SiO$_x$:H layers are shown in white. The active λ/2 central layer of silicon rich a-SiN$_x$:H is shown in gray. The following figure shows a scanning electron microgram (SEM) of the dielectric silicon rich a-SiN$_x$:H microcavity.

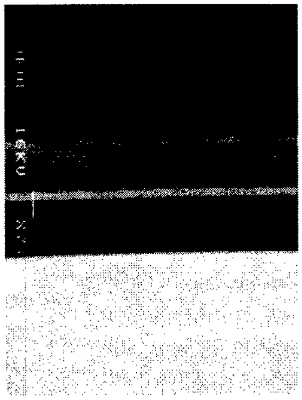

Figure 5.13. The SEM of the dielectric silicon rich a-SiN$_x$:H microcavity.

5.10. Reflectance of the dielectric distributed Bragg reflector

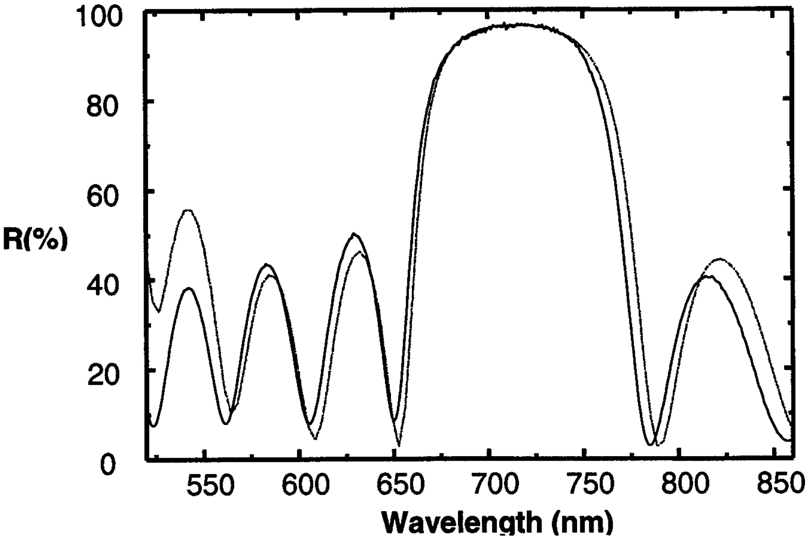

Figure 5.14. Experimental (solid line) and calculated (dotted line) reflectance spectra of a DBR with alternating a-SiN$_x$:H and a-SiN$_x$:H.

Experimental and calculated reflectance spectra of a DBR which has alternating a-SiN$_x$:H and a-SiN$_x$:H layers is shown in the previous figure. The DBR is highly reflective over a stop band range of 80 nm. Calculations are performed by transfer matrix method (TMM). The following figure shows the reflectance spectra of the half wavelength microcavity formed by 2 DBR mirrors.

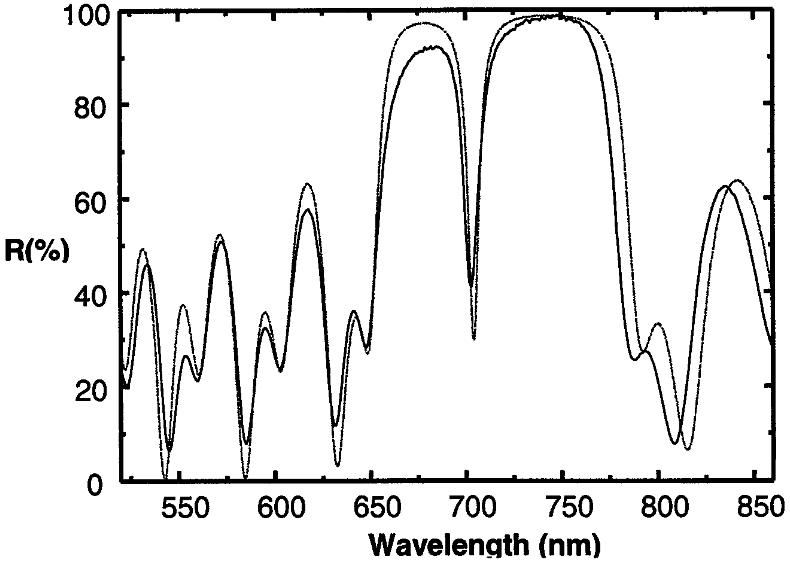

Figure 5.15. Experimental (solid line) and calculated (dotted line) reflectance spectra of half wavelength thick microcavity formed by 2 DBR mirrors.

5.11. Reflectance of the half wavelength thick dielectric microcavity

Experimental and calculated reflectance spectra of a half wavelength thick dielectric microcavity with 2 DBR mirrors is shown in the previous figure. Cavity resonance wavelength is 710 nm, which is the position of the dip in the stopband.

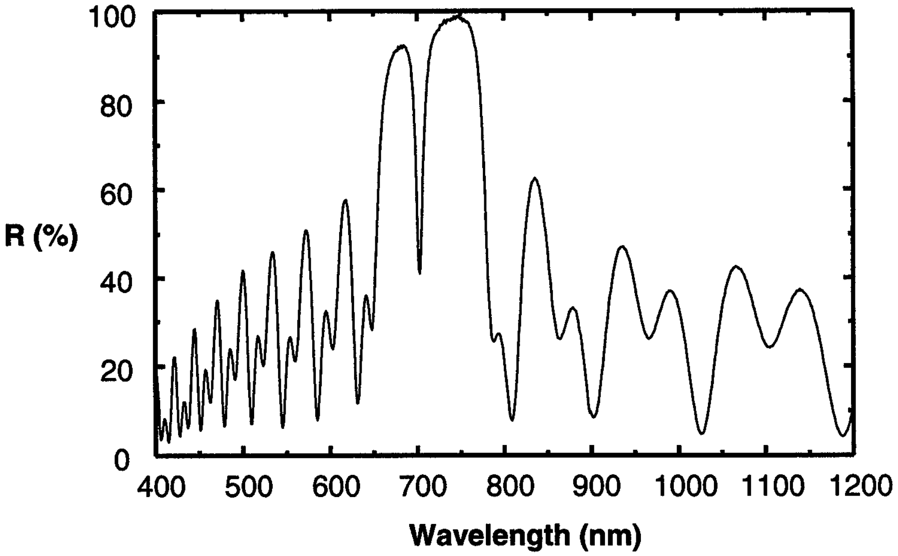

Figure 5.16. Wavelength reflectance spectrum of half wavelength thick microcavity.

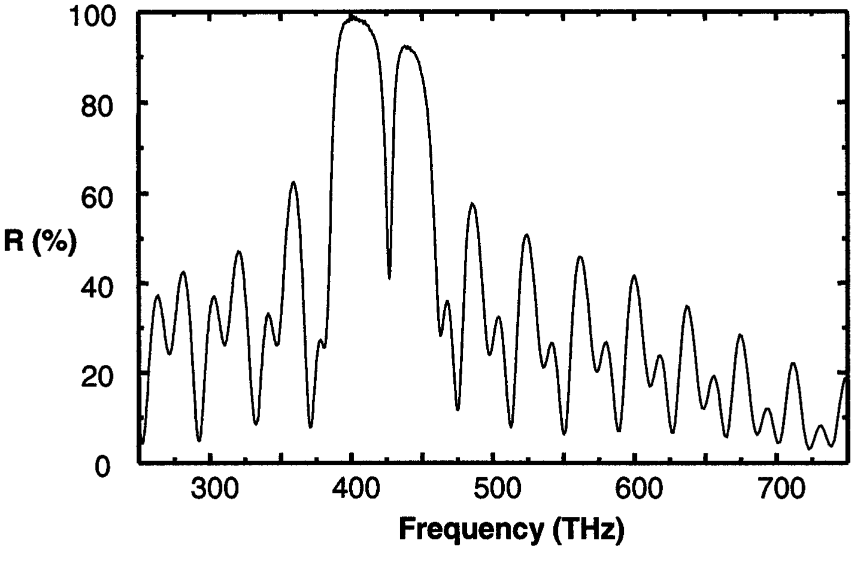

Figure 5.17. Frequency reflectance spectrum of half wavelength thick microcavity.

Reflectance vs. wavelength and frequency spectrum of a half wavelength thick microcavity enclosed between two DBR's, which have alternating a-SiN$_x$:H and a-SiO$_x$:H layers is shown in the previous figures. Reflectance versus frequency spectrum is symmetrical because the adjacent reflection minima and maxima are equally spaced in frequency scale.

The following figure shows the measured reflectance spectrum of the silicon rich a-SiN$_x$:H microcavity. The room temperature reflectance measurements were made at 0±5° with respect to the surface normal with a resolution of 0.1 nm. The measured reflectance spectra of show a microcavity resonance at a wavelength of 710 nm. This resonance has a linewidth of $\Delta\lambda$ = 6 nm and a quality factor of Q = 120. In order to compare our experimental reflectance measurements, we have also calculated the room temperature reflectance spectrum of the a-SiN$_x$:H microcavity using transfer matrix model (TMM) . [101]

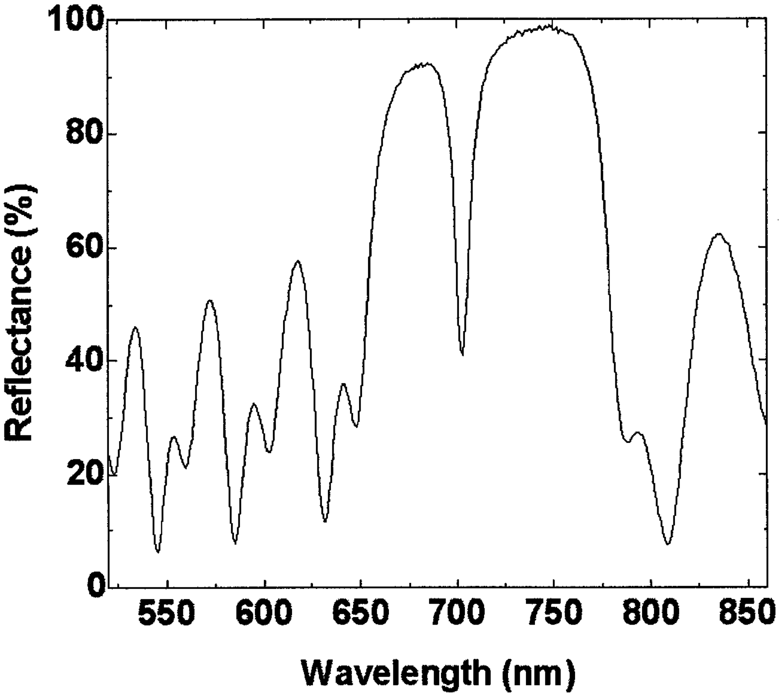

Figure 5.18. The measured reflectance spectrum of the dielectric silicon rich a-SiN$_x$:H microcavity.

The following figure shows the calculated room temperature reflectance spectrum of the dielectric silicon rich a-SiN$_x$:H microcavity. The calculated spectrum is in good agreement with the experimentally observed reflectance spectrum. The resonance linewidth $\Delta\lambda$ and the quality factor Q can also be estimated using the multiplication of the electric field amplitude reflectivity coefficients r_1 and r_2:

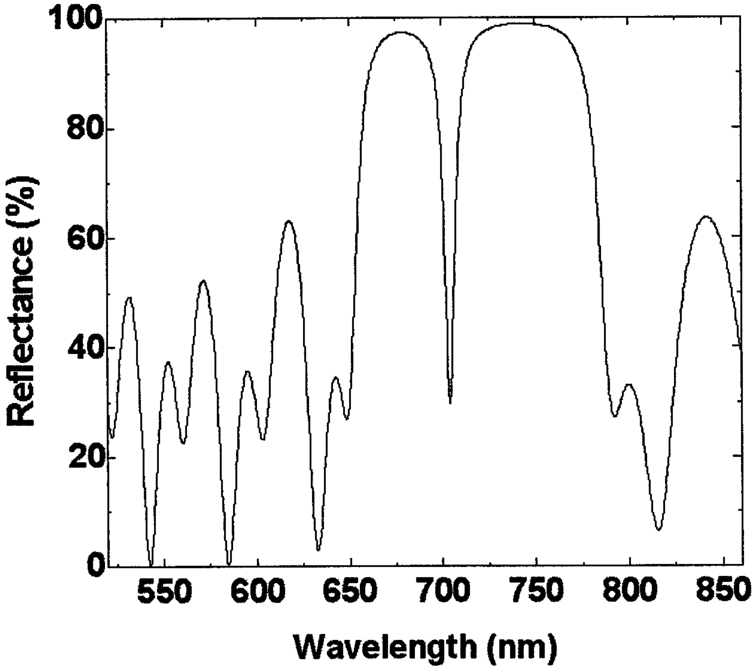

Figure 5.19. The calculated reflectance spectrum of the dielectric silicon rich a-SiN$_x$:H microcavity.

$$r_1 r_2 = \frac{\left(\frac{n_s}{n_{si}}\left(\frac{n_o}{n_n}\right)^{2q}-1\right)\left(\frac{n_s}{n_a}\left(\frac{n_o}{n_n}\right)^{2q}-1\right)}{\left(\frac{n_s}{n_{si}}\left(\frac{n_o}{n_n}\right)^{2q}+1\right)\left(\frac{n_s}{n_a}\left(\frac{n_o}{n_n}\right)^{2q}+1\right)} \qquad ,$$

$$Q = \frac{2\pi\left(1+\frac{n}{\Delta n}\right)}{\ln(1/r_1 r_2)} \qquad ,$$

$$\Delta\lambda = \frac{\lambda}{Q} \qquad ,$$

where $\lambda = 710$ nm is the resonant wavelength, $n_s = 2.03$ the refractive index of the silicon rich a-SiN$_x$:H, $n_{si} = 3.77$ the refractive index of the silicon substrate, $n_a = 1.0$ the refractive index of air, $n_n = 1.72$ the refractive index of the nitrogen rich a-SiN$_x$:H, $n_o = 1.45$ the refractive index of a-SiO$_x$:H, $n = 1.59$ the average refractive index of a-SiN$_x$:H and a-SiO$_x$:H, $\Delta n = 0.27$ the refractive index difference of a-SiN$_x$:H and a-SiO$_x$:H, and q the number of pairs in each DBR.

5.12. PL of the half wavelength thick dielectric microcavity

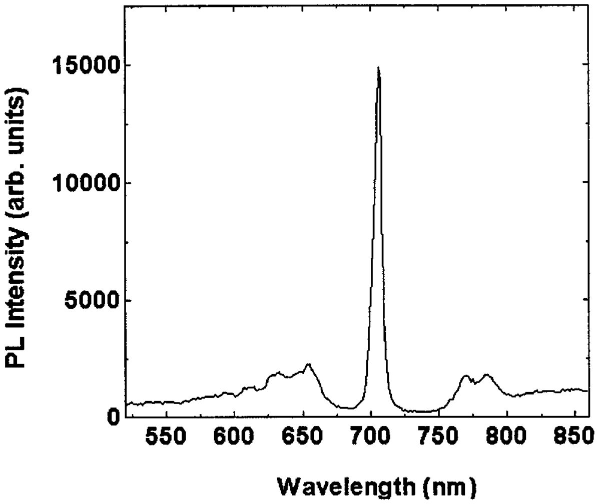

Figure 5.20. The measured PL spectrum of the half wavelength thick dielectric silicon rich a-SiN_x:H microcavity.

The room temperature PL spectra were measured with a resolution of 0.1 nm. The PL spectra were later corrected for the responsivity of the spectrometer and the photomultiplier tube (PMT). The PL spectra were taken at 0±5° with respect to the surface normal. The PL spectra shows a microcavity resonance at a wavelength of 710 nm. This resonance has a linewidth of $\Delta\lambda$ = 6 nm and a quality factor of Q = 120. The PL is enhanced by the microcavity resonance.

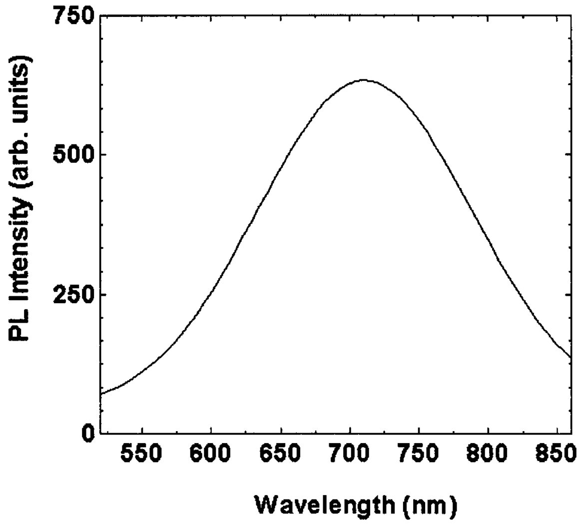

Figure 5.21. The PL spectrum of the half wavelength thick bulk Si rich a-SiN_x:H.

In order to clarify the effect of the microcavity and to demonstrate its advantages with respect to the bulk Si rich a-SiNx:H, we also show the PL of a $\lambda/2$ thick layer of bulk Si rich a-SiNx:H in the previous figure. Both spectra are obtained under the same experimental conditions. The red-near-infrared PL of the bulk Si rich a-SiNx:H has a broad linewidth of 250 nm. This broad linewidth shows that, Si rich a-SiNx:H has potential as a novel photonic gain medium.

A comparison of the spectra in the previous figures shows that the effect of the microcavity is twofold: first, the wide emission band (250 nm) is strongly narrowed to 6 nm; second, the resonant enhancement of the peak PL intensity is more than one order of magnitude with respect to the emission of the $\lambda/2$ thick layer of bulk Si rich a-SiNx:H (assuming that all the transmitted excitation light is pumping the active layer in both cases, with a transmittance of approximately 70% at the excitation wavelength for both cases). In addition by choosing the appropriate width of the Si rich a-SiNx:H active layer and DBR's, it is possible to select the emission wavelength of the microcavity by taking advantage of the broad spectral emission of the a-SiNx:H active layer. Both spectra are plotted together in the following figure.

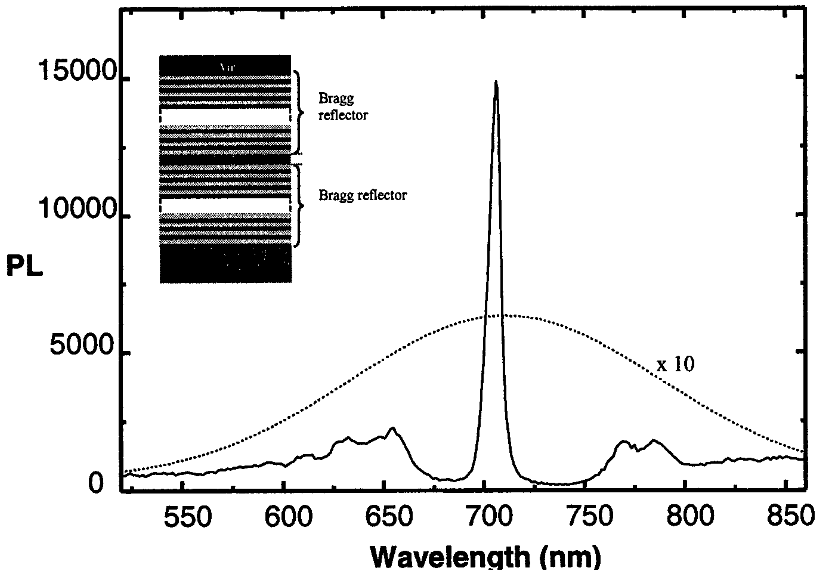

Figure 5.22. Photoluminescence spectrum of a half wavelength thick microcavity with 2 DBR mirrors (solid line) and bulk amorphous silicon (dotted line). The data of the amorphous silicon were multiplied by 10 for comparison. The inset shows the schematic of the structure.

The following figure shows the reflectance and the PL spectra of a half wavelength thick microcavity with DBR's. The PL peak and the dip of the reflectance spectrum coincide at 710 nm. The resonant transmission bandwidth is 6 nm. The PL peak has a full width at half maximum of 6 nm. Q was estimated to be 313 for a microcavity with 2 DBR mirrors, but that was calculated by taking the reflectances of the mirrors as 99.1 %, which is the reflectance maximum of the DBR's. However the fabricated structure's reflectivity is 98%. This gives a quality factor of 155, which is close to the experimental value of 120.

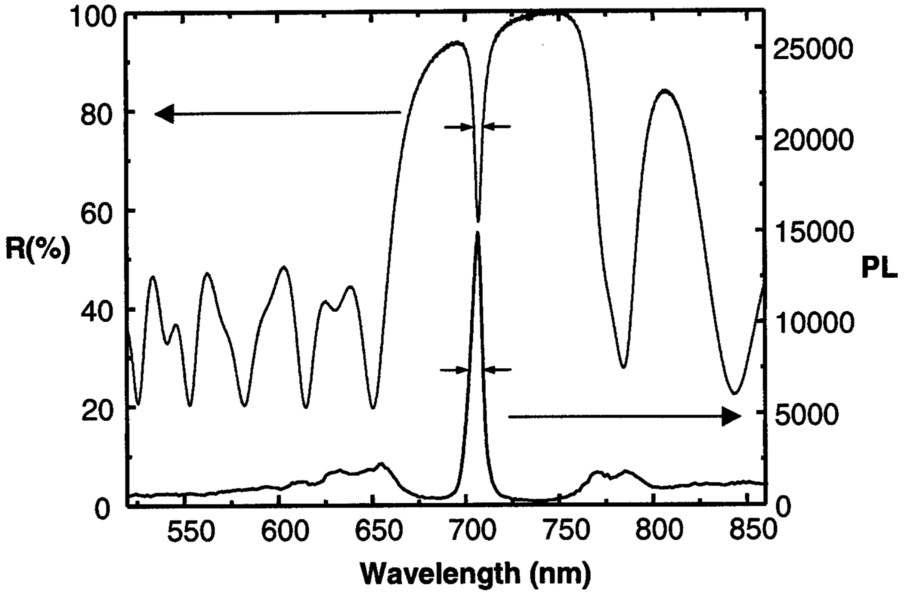

Figure 5.23. Reflectance and PL spectra of a half wavelength thick dielectric microcavity.

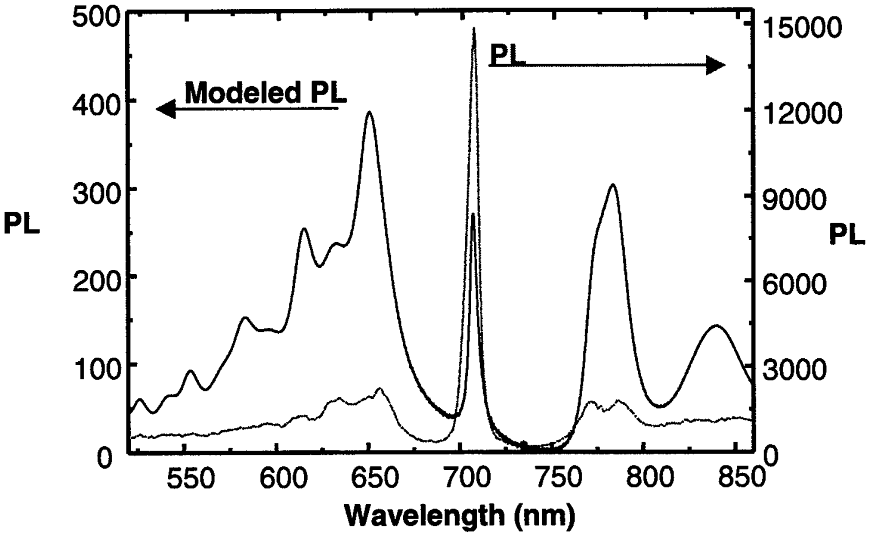

Figure 5.24. Modeled emission spectra (solid line) and PL (dotted line) of a half wavelength thick dielectric microcavity.

In order to prove that the microcavity structure does not act to simply filter the SE, which would yield only a relative and not an absolute enhancement the emission spectrum of a half wavelength thick microcavity was modeled as the PL spectrum of the bulk amorphous silicon multiplied by the transmission spectrum of the sample. The spectral shape of PL can not be reproduced by simply multiplying the PL spectrum of the bulk by the transmittance of the sample.

5.13. Reflectance of the full wavelength thick dielectric microcavity

The thickness of the resonator must be an integer multiple of half wavelength ($\lambda/2$) in order for a resonance to occur. A structure with one λ thick active layer was fabricated, and its optical response was compared to the $\lambda/2$ thick microcavity. The following figures show the reflectance spectra of the λ and $\lambda/2$ thick structures, respectively. As it is seen in the figures, there is not a significant change related to the larger active layer thickness.

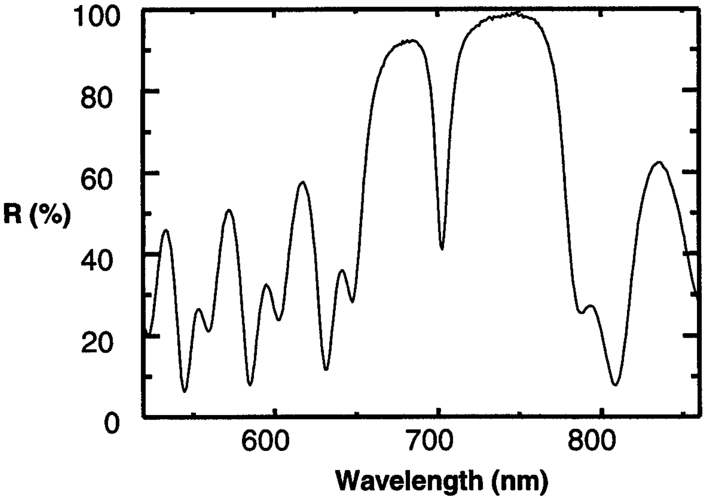

Figure 5.25. Reflectance spectrum of the half wavelength thick cavity.

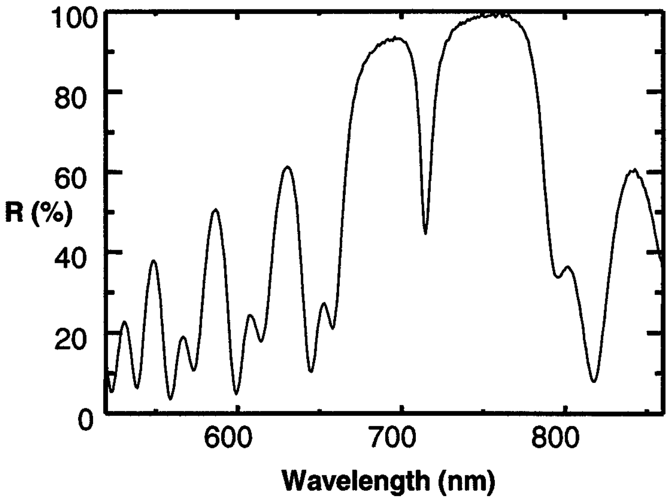

Figure 5.26.Reflectance spectrum of the full wavelength thick cavity.

5.14. PL of the full wavelength thick dielectric microcavity

The following figures show the PL spectra of the half wavelength (λ/2) thick and the full wavelength (λ) thick structures, respectively. As it is seen in the figures there is not a significant change related to the larger active thickness.

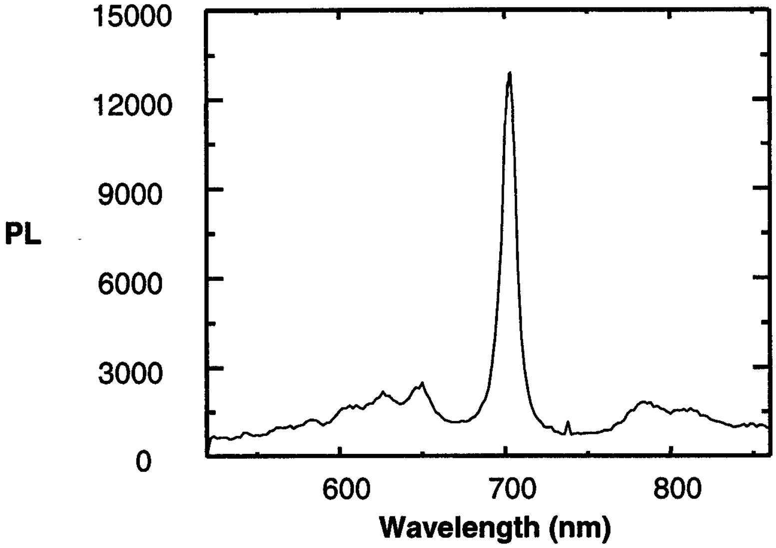

Figure 5.27. PL spectrum of the half wavelength thick cavity.

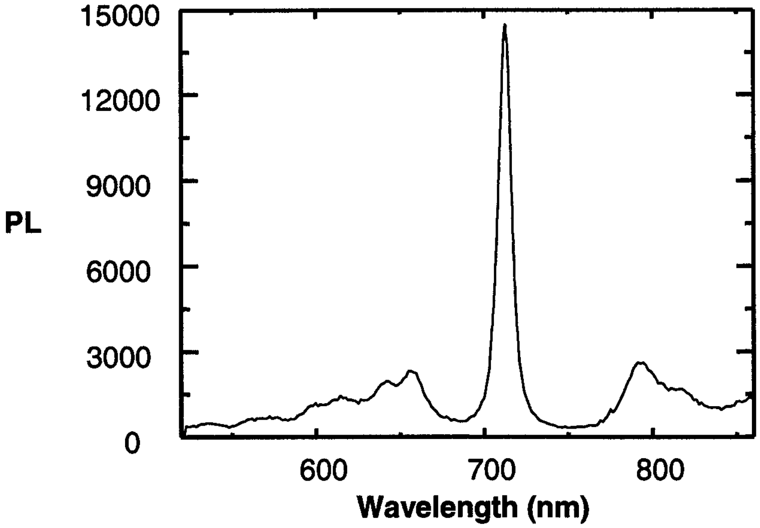

Figure 5.28.PL spectrum of the full wavelength thick cavity.

5.15. References

[97] B.J. Clark, T. Frost, and M.A. Russel, “UV Spectroscopy Techniques: Instrumentation, and Data Handling", in “Techniques in Visible and Ultraviolet Spectrometry,” Vol. 4 (Chapman & Hall, London, 1993).

[98] H.G. Kim, K.H. Park, B.N. Park, H.J. Lim, S.K. Min, H.L. Park, W.T. Kim, Jap. J. Appl. Phys. **32**, 476 (1993).

[99] V. Capozzi, Phys. Rev. B **28** 4620 (1983).

[100] T. Schmidt, K. Lischka, W. Zulehner, Phys. Rev. B **45** 8989 (1992).

[101] M. Born and E. Wolf, “Principles of Optics,” (Cambridge University Press, Cambridge, 1998) p. 51

6. Conclusions

Bulk and microcavity luminescence properties of hydrogenated amorphous silicon nitride (a-SiN_x:H) were studied at room temperature and at low temperatures. The PL emission intensity increases at low temperatures due to the lack of thermally excited phonons. The emission spectrum stays broad even at low temperatures. The broad luminescence spectrum even at low temperatures is a results of the heterogenous size distribution of the amorphous silicon quantum dots. This heterogenous size distribution is further confirmed by atomic force microscopy (AFM) measurements of the sample surface. The photoluminescence (PL) extends from the red part of the spectrum to the near-infrared for the samples grown without ammonia (NH_3). The PL is in the blue-green part of the spectrum for the samples grown with NH_3.

These complementary colors cover the whole visible spectrum, herald the possibility of an a-SiN_x:H color flat panel display. The broad PL spectrum of the a-SiN_x:H, also makes it a suitable source for wavelength division multiplexing (WDM) applications.

Metallic and dielectric Fabry-Perot microcavities are used for the enhancement and inhibition of PL in a-SiN_x:H. The microcavity mode was tuned to the emission maximum of a-SiN_x:H (710 nm). The reflectance and the PL measurements show the effect of the microcavity. The a-SiN_x:H microcavities consist of an active (a-SiN_x:H) layer sandwiched between two mirrors. The metallic microcavity was realized by a metallic back mirror and an a-SiN_x:H - air or a metallic front mirror. Dielectric microcavities were realized using distributed Bragg reflectors (DBR's). This is the same structure used in vertical cavity surface emitting lasers (VCSEL's). Stopband widths of 80 nm and 99% reflection at the middle of the stopbands were obtained by using alternating quarter wavelength thick a-SiO_x:H and a-SiN_x:H layers. The DBR's were fabricated using alternating layers of quarter wavelength thick a-SiN_x:H and a-SiO_x:H.

The reflectance spectra were simulated by the transfer matrix method (TMM). Excellent agreement between the theoretical and experimental spectra was obtained. The effect of the number of top mirror layer pairs on the emission maximum and the transmittance at the microcavity resonance was investigated both theoretically and experimentally. The reflectance of the DBR increases as the number of layer pairs in the dielectric stack increases. This, in turn, reduces the emission maximum and the transmittance at the cavity resonance, because of the reduced light coupling out of the microcavity. A microcavity with one wavelength thick active layer was also fabricated and the same cavity effects were demonstrated.

The PL of the bulk a-SiN_x:H is enhanced at, and inhibited in between, the resonances of the microcavity, with respect to the bulk a-SiN_x:H. The enhancement and inhibition of the PL is understood by the modified photon density of states (DOS) of the microcavity. The PL bandwidth was narrowed to a linewidth of 6 nm, with respect to the linewidth of the bulk a-SiN_x:H, again due to the presence of the electromagnetic modes of the microcavity. Quality factors as high as 120 was obtained. This narrowing and enhancement of the PL can be understood by the redistribution of the density of optical modes due to the presence of the microcavity. The microcavity enhancement and inhibition of luminescence in a-SiN_x:H opens up a variety of possibilities for optoelectronic applications such as color flat panel displays or resonant cavity enhanced (RCE) devices for WDM applications.

Federal Acquisition Regulation Clauses

(1) In accordance with Defense Federal Acquisition Regulation 252.227-7036, Declaration of Technical Data Conformity (Jan 1997), All technical data delivered under this contract shall be accompanied by the following written declaration:

"The Contractor, Koc University, hereby declares that, to the best of its knowledge and belief, the technical data delivered herewith under Contract No. F61775-01-WE062 is complete, accurate, and complies with all requirements of the contract."

DATE: November 25, 2002

Name and Title of Authorized Official: Dr. Ersin Yurtsever, Professor and Dean

(End of Clause)

(2) In accordance with the requirements in Federal Acquisition Regulation 52.227-13, Patent Rights-Acquisition by the U.S. Government (Jun 1989), CONTRACTOR WILL INCLUDE IN THE FINAL REPORT ONE OF THE FOLLOWING STATEMENTS:

(A) "Disclosures of all subject inventions as defined in FAR 52.227-13 have been reported in accordance with this clause."

DATE: November 25, 2002

Name and Title of Authorized Official: Dr. Ersin Yurtsever, Professor and Dean

(End of Clause)